

In compliance with the
Canadian Privacy Legislation
some supporting forms
may have been removed from
this dissertation.

While these forms may be included
in the document page count,
their removal does not represent
any loss of content from the dissertation.

The Effect of the Injection Scale
on Scalar Mixing in the Turbulent Wake
of a Circular Cylinder.

Sébastien Beaulac

Department of Mechanical Engineering
McGill University
Montreal, Quebec, Canada

A thesis submitted to the Faculty of Graduate Studies and Research
in partial fulfilment of the requirements for the degree of
Master of Engineering

©Sébastien Beaulac, Montreal, Canada, 2003



National Library
of Canada

Bibliothèque nationale
du Canada

Acquisitions and
Bibliographic Services

Acquisisitons et
services bibliographiques

395 Wellington Street
Ottawa ON K1A 0N4
Canada

395, rue Wellington
Ottawa ON K1A 0N4
Canada

Your file *Votre référence*

ISBN: 0-612-88344-2

Our file *Notre référence*

ISBN: 0-612-88344-2

The author has granted a non-exclusive licence allowing the National Library of Canada to reproduce, loan, distribute or sell copies of this thesis in microform, paper or electronic formats.

L'auteur a accordé une licence non exclusive permettant à la Bibliothèque nationale du Canada de reproduire, prêter, distribuer ou vendre des copies de cette thèse sous la forme de microfiche/film, de reproduction sur papier ou sur format électronique.

The author retains ownership of the copyright in this thesis. Neither the thesis nor substantial extracts from it may be printed or otherwise reproduced without the author's permission.

L'auteur conserve la propriété du droit d'auteur qui protège cette thèse. Ni la thèse ni des extraits substantiels de celle-ci ne doivent être imprimés ou autrement reproduits sans son autorisation.

Canada

Abstract

The effect of the ratio of the velocity field integral scale at the injection point to the scalar injection scale (the injection ratio) on the mixing of a passive scalar (temperature) is studied in the wake of a circular cylinder. Hot-wire anemometry and cold-wire thermometry are used to measure simultaneously the velocity and thermal fields, respectively. A mandoline is used to (slightly) heat the wake.

The injection ratio is varied in two ways. The velocity integral scale at the injection point is varied by changing the mandoline downstream position. Increasing the velocity scale, ℓ_o (i.e., increasing the mandoline downstream position), increases the rate at which the scalar variance decays and reduces the integral length scale of the scalar. The time scale ratio ($r = (\langle q^2 \rangle / \epsilon) / (\langle \theta^2 \rangle / \epsilon_\theta)$) decreases with increasing ℓ_o , in agreement with experiments done in homogeneous and isotropic turbulence.

The scalar injection scale is varied by changing the width, w , of the mandoline. Increasing w decreases the decay rate of the scalar variance, which is analogous to increasing the wire spacing in grid-generated turbulence. The integral length scale of the scalar field (both longitudinal and transverse) and the time scale ratio are, however, not affected by w , in contrast with experiments done in homogeneous and isotropic turbulence.

Résumé

Ce mémoire traite de l'effet du rapport de l'échelle intégrale de longueur du champ de vitesse au point d'injection et de l'échelle d'injection scalaire (le rapport d'injection) sur le mélange des scalaires passifs dans le sillage d'un cylindre circulaire. Les champs de vitesse et de température sont mesurés par l'anémométrie à fil chaud et la thermométrie à fil froid, respectivement. Une mandoline est utilisée pour chauffer (légèrement) le sillage.

Le rapport d'injection est varié en deux façons. L'échelle du champ de vitesse, ℓ_o , est variée en changeant la position de la mandoline en aval du cylindre. En augmentant ℓ_o (c'est à dire la position de la mandoline en aval du cylindre), le déclin de la variance scalaire est accéléré et l'échelle intégrale du champ scalaire est diminuée. Le rapport des échelles de temps ($r = (\langle q^2 \rangle / \epsilon) / (\langle \theta^2 \rangle / \epsilon_\theta)$) diminue si ℓ_o augmente, en accord avec les résultats obtenus en turbulence homogène et isotrope.

L'échelle du scalaire est variée en changeant la largeur, w , de la mandoline. Le déclin de la variance scalaire ralentit si w est augmentée parce que cela a pour effet de diminuer le rapport d'injection. L'échelle intégrale du champ scalaire (longitudinale et transversale) ainsi que le rapport des échelles de temps ne sont, par contre, pas affectés par w , contrairement aux expériences réalisées en turbulence homogène et isotrope.

Acknowledgements

First, I would like to express my gratitude to Professor Mydlarski for his support and encouragement throughout the work for this thesis. He has been a great source of inspiration and was always available to help me progress in my work.

Also, I would like to thank the National Science and Engineering Research Council of Canada for their support through the Post-Graduate Scholarships program.

Finally, I am thankful to Marie-Chantal Pellerin and Olivier Shareck for the great support they provided during my work.

Contents

1	Introduction	10
1.1	Literature Review	12
1.1.1	Passive Scalars	12
1.1.2	The Heated Wake of a Circular Cylinder	14
1.1.3	Effect of the Initial Conditions	14
1.2	Objective of this Work	15
2	Experimental Setup	17
2.1	Wind Tunnel Facility	17
2.2	Heat Injection Mechanisms	17
2.3	Measurement Instruments	19
2.4	Calibration Procedures	21
2.4.1	Cold-Wire Calibration	21
2.4.2	Hot-Wire Calibration	24
2.5	Data Acquisition and Analysis	27
3	Flow Field	30
3.1	Velocity	30
3.1.1	Structure of the Hydrodynamic Wake	31
3.1.2	Influence of the Mandoline on the Flow	33
3.1.3	Effect of the Scalar	37
3.2	Temperature	39
3.2.1	Structure of the Thermal Wake	39

4	The Effect of the Velocity Integral Scale on the Scalar Field	43
4.1	Evolution of the Velocity Integral Scale	44
4.2	Decay Rate of the Scalar Variance	45
4.3	Structure of the Scalar Field	48
4.4	Time Scale Ratio	51
4.5	Longitudinal Velocity-Scalar Correlation	55
5	The Effect of the Scalar Injection Scale on its Field	58
5.1	Decay Rate of the Scalar Variance	60
5.2	Structure of the Scalar Field	61
5.3	Time Scale Ratio	66
6	Conclusions	68
6.1	Future Work	69
A	Accuracy of the IFA300 Constant Temperature Anemometer	71
A.1	Effect of the Operating Resistance	71
A.2	Variations in R_p	72
A.3	Selecting the Proper Operating Resistance.	73
	A.3.1 Isothermal Flows.	74
	A.3.2 Non-Isothermal Flows.	74
A.4	Rounding Errors	76

List of Figures

2.1	Physical parameters used to specify a mandoline configuration.	18
2.2	Velocity and temperature probe arrangement.	20
2.3	Power spectral density of the temperature field.	22
2.4	Calibration curve for a cold-wire.	23
2.5	Response of a cold-wire to the current injection technique.	24
2.6	Calibration curves for a hot-wire at different flow temperature.	26
2.7	Effect of the frequency correction on the dissipation spectra.	29
3.1	Longitudinal mean velocity profile.	32
3.2	RMS of the velocity fluctuations.	32
3.3	Mean velocity profile for different heights.	33
3.4	RMS profile of v for different heights.	34
3.5	Power spectral density of u for different heights.	34
3.6	Effect of the mandoline on the power spectral density of u	36
3.7	Effect of the temperature on the power spectral density of v	38
3.8	Mean temperature excess profile.	40
3.9	Profile of the RMS of temperature fluctuations.	40
3.10	RMS profile of T for different heights.	41
3.11	Power spectral density of T for different heights.	42
4.1	Evolution of the integral length scale of u downstream of the cylinder.	44
4.2	Decay of the variance of u downstream of the cylinder for the entire range of x/D	45
4.3	Decay of the velocity variance for the range under consideration herein.	46
4.4	Decay of the temperature variance as a function of mandoline downstream position.	47

4.5	Decay rate exponent as a function of mandoline downstream position.	48
4.6	Auto-correlation of the temperature signal.	49
4.7	Spectra of the temperature field for different mandoline downstream positions.	50
4.8	Spectra multiplied by the wavenumber for different mandoline downstream positions.	51
4.9	The decay exponent as a function of the wavenumber at the peak of $k_1 \times E_\theta$	52
4.10	Decay of the scalar variance dissipation rate as a function of mandoline downstream position.	53
4.11	The time scale ratio r as a function of downstream position.	54
4.12	The time scale ratio r as a function of the ratio of the velocity to scalar integral length scales.	55
4.13	The spectrum multiplied by the wavenumber for different mandoline downstream positions.	56
4.14	The cross-correlation coefficient as a function of downstream position.	56
4.15	The coherence of the temperature field as a function of mandoline downstream position.	57
5.1	Typical time histories of u	59
5.2	The effect of the w on the decay rate of $\langle \theta^2 \rangle$	60
5.3	The decay rate as a function of the width of the mandoline.	61
5.4	The auto-correlation of temperature for the three different mandoline widths.	62
5.5	Spectrum multiplied by the wavenumber for different mandoline widths.	62
5.6	The transverse auto-correlation of u	63
5.7	The transverse auto-correlation of T for the cylinder.	64
5.8	The transverse auto-correlation of T for different mandoline downstream positions.	65
5.9	The transverse auto-correlation of T for different mandoline widths.	65
5.10	The downstream evolution of the time scale ratio for different mandoline widths.	67
A.1	Effect of R_{op} on velocity output.	72
A.2	Schematic of a hot-wire velocity probe.	73

A.3	Calibration curves for a hot-wire keeping its operating resistance constant.	74
A.4	Calibration curves for a hot-wire keeping its overheat ratio and the flow temperature constant.	75
A.5	Calibration curves for a hot-wire at constant flow temperature and adjusting the overheat for changes in ambient temperature.	76

List of Tables

2.1	Typical calibration constants for the two channels of an X-wire.	26
3.1	Principal velocity length scales of the flow.	30
3.2	Effect of the temperature on the important velocity length scales.	37
4.1	Effect of the mandoline's downstream position on ℓ_θ	49
4.2	The decay exponents of the scalar variance and its dissipation rate.	54
5.1	Comparison between the longitudinal and the transverse integral length scale of the scalar field.	66

Chapter 1

Introduction

Fluid mechanics plays an important role in the wide variety of present-day engineering applications. In many of these applications, the working fluid has a very low viscosity such that its motion is almost always turbulent. It is therefore of great importance to fully understand the dynamics of a turbulent flow, a task that is made difficult by its complex, three-dimensional, chaotic nature.

Although turbulent flows are more difficult to tackle than laminar ones, in many engineering applications, the flow is forced to be turbulent to benefit from its ability to mix momentum, heat, and mass very rapidly. A well-known example of turbulent momentum mixing is the presence of dimples on a golf ball: by forcing the boundary layer to become turbulent, the point of boundary layer separation is pushed back due to the increase in the boundary layer's momentum. Consequently the pressure drag (and therefore total drag) is reduced and the distance that the golf ball flies is increased. In heat transfer, the flow through heat exchangers is generally turbulent to increase the mixing and, therefore, the amount of heat that is transferred to (or from) the flow. In fuel injection systems, the mixing of the fuel with the oxidizer is very important for fast and complete combustion, so the oxidizer is often in turbulent motion.

On the other hand, turbulence can occur naturally. The turbulent motion of the earth's boundary layer affects many engineering applications. The flow in rivers is always turbulent. This turbulence also affects scalar mixing phenomena. In meteorology, the knowledge of the air's humidity and temperature is made difficult by the turbulent motion of the earth's boundary layer, which renders weather forecasting difficult. In telecommunications, the propagation of electromagnetic waves is affected by the refractive index of the atmosphere, which depends on its temperature and humidity. The turbulent motion of oceanic mixed layer is affected by its salinity and

temperature. Moreover, the turbulence of the atmosphere greatly enhances the dispersion of pollutants from smoke stacks and therefore inhibits the accumulation of high-levels of pollutant concentrations.

As can be seen in the previous discussion, a number of applications involve the mixing of a scalar in a turbulent flow. Be it temperature or a contaminant (e.g., salt in water or moisture in air), the equation governing the mixing of the scalar (assuming constant properties of the scalar) takes the same form:

$$\frac{\partial \theta}{\partial t} + \vec{V} \cdot \vec{\nabla} \theta = \gamma \nabla^2 \theta \quad (1.1)$$

where γ is the scalar diffusivity. In addition, if the presence of the scalar has a negligible effect on the velocity field, it is said to be passive. In many applications, this is indeed the case. For small enough temperature variations, buoyancy forces can be negligible compared with inertia forces so that temperature is effectively a passive scalar. It is thus insightful to study the mixing of small temperature differences in air.

A fundamental feature of turbulent flows is that they have a continuous distribution of scales. The turbulent kinetic energy is supplied by the largest scales of the flow. Given that the Reynolds number ($Re = UL/\nu$) is typically large, the viscosity is not important at the largest scales. Therefore, the largest eddies break down into smaller and smaller eddies until their Re is small (where both L and U are characteristic of an eddy). At this scale, which is defined as the Kolmogorov scale (also called the dissipation scale), viscosity becomes important, and the kinetic energy is converted into internal energy. This is often referred to as the turbulent cascade of energy. In many industrial flows, Re is large so that the small scales of the flow are so small and pass by a measurement probe so fast that they are difficult to capture. This complicates the computation of small-scale statistics, such as dissipation, and these important quantities often have to be deduced from large-scale quantities.

It is therefore of prime interest to gain a better understanding of the interaction between the large and small scales of a passive scalar in fundamental flows. A basic method to this end is to hold the velocity field constant and vary the initial conditions of the scalar injection. This has been done in grid generated turbulence (i.e., homogeneous and isotropic turbulence) using a mandoline. A mandoline consists of an array of parallel, fine, electrically heated wires that presumably do not disturb the velocity field. Because the mandoline is separated from the source of the turbulence, it is possible to vary the ratio of the velocity integral length scale at the injection

point to the scalar injection scale by varying the mandoline's wire separation or its downstream position. Interesting and useful insight has been gained following this method. Hence, the objective of the present study is to advance the success of this method by relaxing the homogeneous and isotropic constraints of the flow by studying a free shear flow, viz., the wake of a circular cylinder.

1.1 Literature Review

Turbulence includes a large portion of fluid dynamics research. Numerous books have been written on fluid dynamics: White[1], Batchelor[2], and even an encyclopedia has been published[3]. For viscous laminar flows, details are given by White[4]. Heat transfer in moving fluids is called convective heat transfer and is treated by Bejan[5], and Kays and Crawford[6]. Since the equations of motion for fluids are non-linear, there exist multiple solutions for a given problem. The stability of these solutions can be studied and details for the simplest flows, laminar flows, are given in Swinney and Gollub[7], and Huerre and Monkewitz[8]. It is known that when inertia forces in the fluid are large compared to the viscous forces, laminar flows will be unstable. The ratio of these two forces is defined as the Reynolds number (Re). Therefore turbulence, which is the result of instabilities in the fluid, is more likely to occur for large Reynolds numbers. Turbulence has been studied for more than a century and its scaling analysis and physical description are presented in Tennekes and Lumley[9] and Pope[10]. Unfortunately, such approaches are restricted to simple flows. For flows that are less simple, mathematical models can help, as can numerical simulations[11].

1.1.1 Passive Scalars

Passive scalar mixing in turbulent flows is a problem that has received a great interest over the last part of the century[12]. Be it temperature, chemical species concentration, salt in water, or humidity in air, the differential equation governing these quantities is of the same mathematical form[5, 6]. The implication of the adjective passive is that the scalar does not disturb the velocity field in which it is being transported. For high concentrations of salt in water, the mixture's density is changed, therefore creating gradients in the density of water, which affect the flow field when in the presence of a gravitational field. Temperature too, can change the flow by buoyancy effects[13]. However, when the range of temperatures in the flow field is small, the buoyancy force can be negligible compared to other forces driving

the flow. Thus temperature can be treated as passive in special cases.

The passive scalar problem can be studied in several ways. The recent developments in computing technologies promote the use of numerical simulations. The most fundamental technique is Direct Numerical Simulation (DNS)[14]. It consists of solving the instantaneous Navier-Stokes equations and requires significant computing power because every detail of the flow is computed, i.e., it computes all the scales of the flow. Another technique, Large Eddy Simulation (LES)[15], consists of computing the largest scales of the flow down to a specified sub-grid size. It employs models to account for the effect of the smaller scales on the large ones. Other techniques compute only mean values, like the dissipation rate of turbulent kinetic energy or the mean flow velocity, for example. They use the Reynolds averaged equations and apply models to the unknown terms. Lastly, some researchers have tried to develop new theoretical approaches applicable to mixing phenomena[16, 17].

Another way to study scalar mixing problems is to perform experiments. A number of methods exist to measure the scalar field. One of them is to record a time history of temperature fluctuations at some point of interest using Cold-Wire Thermometry (CWT)[18]. Another popular method is to take a picture of chemical concentrations in water using Laser Induced Fluorescence (LIF)[20]. To vary the Schmidt number ($Sc = \frac{\nu}{\gamma}$), one can either change the scalar (if LIF is used) or change the ambient fluid if CWT is used (some researchers have done experiments in low-temperature helium instead of air[19]).

Experiments have been performed to study scalar mixing problems in basic flows. The simplest turbulent flow is homogeneous and isotropic. The closest experimental reproduction of this flow occurs by passing a uniform flow through a homogeneous grid. Scalar fluctuations can be introduced in the flow by different methods such as heating the grid itself[22, 23], placing an array of parallel heated wires downstream of the grid (a mandoline)[24] or imposing a mean temperature gradient on the flow[25]. Homogeneous, isotropic turbulence is the simplest flow since there is no mean velocity gradient and is therefore shear-free. There are different classes of flows that contain shear, the simplest being homogeneous shear flow[27]. There is also a class of shear flows that are wall-bounded. They include flows like boundary layers[26, 28, 29] and channel flows[30, 31]. Lastly, free-shear flows such as jets[32, 33, 34], mixing layers[35], and wakes form another common class of flows.

1.1.2 The Heated Wake of a Circular Cylinder

The wake generated by a circular cylinder is the most commonly studied wake. The most natural way to generate temperature fluctuations in such a wake is by heating the cylinder itself. The velocity field of the wake evolves rapidly in the downstream direction and can be divided into different regions. Due to experimental limitations, the whole wake cannot generally be studied at once and a choice has to be made regarding the region of interest. The region closest to the cylinder is called the near wake. It spans from the cylinder to $x/D \sim 5$ or 6 [36]. The next region is the intermediate wake which extends to $x/D \sim 80$ [36, 37]. This part has been referred to the primary vortex street-dominated region and its end location is approximately given by the location where the temperature skewness changes sign, from positive to negative[38, 39]. The last part is the self-preserving far wake, which starts at a downstream distance of several hundred of diameters. Different estimates have been obtained for this position and they vary from 100 to 250 diameters[40, 41]. However, for large enough downstream distances, the wake can be assumed to be self-similar[42]. Lastly, it should be noted that the limits separating the wake regions are also functions of Re .

The wakes of bluff bodies, such as circular cylinders, have been shown to possess different inherent structures which are functions of Re . For example, if $40 < Re < 150$, the wake is laminar, but von Kármán vortices are shed. The von Kármán vortex street is also present for turbulent flow. If $300 < Re < 3 \times 10^6$, the turbulent vortices are shed at a constant Strouhal number ($S_t = fD/U_\infty \sim 0.21$)[43]. This important structure of the flow for this Re range has attracted the interest of some experimentalists. For example, Ferré and Giralt[44] found that the entrainment process is accomplished mainly by engulfing external fluid and Matsumura and Antonia[36] studied how the von Kármán vortex street transports the scalar. Antonia and Browne also studied the anisotropy of the temperature dissipation in the wake of a heated cylinder and found it to be high[45]. In addition, because this structure in the wake is not trivial to model numerically, some researchers have developed correlations[37, 42] and more general numerical models.

1.1.3 Effect of the Initial Conditions

The initial length scale at which heat is injected into the turbulent field is of direct importance to the evolution of the scalar field. When the heat source is the same as the turbulence source, for example temperature fluctuations in the wake of a heated

cylinder, the only possible way of varying the initial conditions is to vary the amount of heat introduced in the flow. However, the heat input should not affect the dimensionless characteristics of the temperature field when the temperature fluctuations are passive. Warhaft and Lumley[24] found that in grid generated turbulence, the decay rate of temperature (related to the structure of the large scales) was affected by the amount of heat released by the grid. The most reasonable explanation for this is that, although temperature fluctuations were passive at the measurement locations, they might not be passive close to the grid. They therefore investigated another mechanism to inject the scalar by use of an array of fine parallel heated wires. They called this a *mandoline*. The use of a mandoline is a novel way to separate the heat injection scale from the velocity scale and thus provides a new variable to the initial conditions.

Warhaft and Lumley found that by varying the downstream position of the mandoline relative to the grid, or by varying the wire spacing, it was possible to vary the ratio of the thermal to mechanical time scales. Sreenivasan *et al.*[46], who did the same type of experiments but using a heated screen (like a two-dimensional mandoline), found that the decay exponent of scalar variance (m) was hardly changed by the downstream position of the screen. The downstream position of their screen relative to the grid was, however, larger than used by Warhaft and Lumley. This difference was later reconciled by Durbin[47] using a Lagrangian dispersion theory. He was able to predict m for a given ratio of velocity to temperature scales (ℓ_o/ℓ_θ , ℓ_o being the integral length scale of the velocity field at the scalar injection location). He found that m was affected by ℓ_o/ℓ_θ up to a value of 2.5 after which it would be constant. Given the experimental setup of Warhaft and Lumley[24] and Sreenivasan *et al.*[46], he showed that the former experiment had values of ℓ_o/ℓ_θ from 0.8 to 2.0 and the latter exceeded 2.5. Another important point of comparison between the experiments of Warhaft and Lumley and Sreenivasan *et al.* is that both varied the wire spacing but obtained different results. In the case of Warhaft and Lumley, the variation in wire spacing was always greater than ℓ_o and this produced a discernable effect on m . In contrast, m was constant for Sreenivasan *et al.* when they varied the spacing for values smaller than ℓ_o .

1.2 Objective of this Work

The main objective of this work is to extend the work of Warhaft and Lumley[24] and Sreenivasan *et al.*[46] to the wake of a circular cylinder. A mandoline is to be

used to vary the ratio of the velocity integral length scale at the injection point to the scalar injection scale (ℓ_o/L_θ). The goal is to verify if some flow characteristics of homogeneous and isotropic turbulence, like the power-law decay of the velocity and scalar variances, can be extended to the wake. If such a power-law regime exists, the effect of ℓ_o/L_θ on the decay rate and the structure of the scalar field will be studied. The principal interest is to see how the new terms in the scalar variance budget (the turbulent transport term ($\frac{1}{2} \frac{\partial(\theta^2)}{\partial y}$) and the mean turbulent production term ($\langle v\theta \rangle \frac{\partial T}{\partial y}$)) affect the scalar field (and its decay in particular). Lastly, the longitudinal velocity-scalar correlation will be compared to the results in Warhaft and Lumley to determine whether the mandoline dissociates the velocity and scalar fields, as is the case in grid-generated turbulence.

This thesis is divided in six chapters. The experimental setup and the measurement instruments, as well as their calibration procedure, will be discussed in chapter 2. The third chapter validates the flow and temperature fields. In chapter four, the effects of varying the velocity scale at the injection point are discussed. A discussion on varying the scalar injection scale is elaborated in the fifth chapter. The last chapter concludes the thesis and proposes some extensions to this work.

Chapter 2

Experimental Setup

2.1 Wind Tunnel Facility

The experimental measurements are made in the 3 x 4 foot, low-turbulence intensity wind tunnel located in the Aerodynamic Laboratory of McGill University. The wind tunnel is of the suction type with a 9-to-1 contraction area ratio that follows a fifth degree polynomial contraction profile. The test section is 9 feet long and bevelled corners slowly decrease in length in the downstream direction (thus increasing the cross-sectional area) to maintain a zero pressure gradient flow. The test section is followed by a small-angle diffuser and the axial fan is located downstream of it. The rotational speed of the fan is controlled electronically to within ± 1 rpm, which ensures a good stability (and repeatability) of the mean flow. The experiments were conducted at a mean flow velocity of 10.2 m/s. For this flow rate, the turbulence intensity is of the order of 0.1% away from the walls' boundary-layers, i.e., in the inviscid core of the tunnel.

2.2 Heat Injection Mechanisms

The wake is produced by placing a 1" (25.4 mm) circular cylinder at the entrance of the test section, where the flow is straight and parallel. The cylinder axis is vertically aligned (i.e., in the z-direction). The wake is heated using two different mechanisms. Heating the cylinder itself is one mechanism that has been used in the vast majority of previous studies of the heated wake. The other mechanism consists of an array of heated parallel wires oriented in the same direction as the axis of the cylinder. This more novel heat injection mechanism is called a *mandoline*. The two mechanisms are

never employed simultaneously. Moreover, when the cylinder is heating the flow, the mandoline is removed completely from the wind tunnel.

To maximize the downstream distance at which data can be taken, the cylinder is placed at the entrance of the test section. The apparatus consists of four parts: a 1" (25.4 mm) external diameter aluminum pipe of $\frac{5}{64}$ " (2 mm) wall thickness; an electric heater of one kilowatt maximum power (rated at 120 VAC) with an external diameter of $\frac{1}{4}$ " (6.35 mm); a series of 25 mm (in length) concentric thermal fins that fill the gap between the electric heater and the pipe; and the end supports fixing the cylinder to the walls of the test section. The cylinder is heated using AC power that can be adjusted using a variable AC transformer. A high thermal conductivity paste is added around the thermal fins to ensure a uniform axisymmetric thermal resistance between the electric heater and the outside of the aluminium pipe. The cylinder spans the whole height of the tunnel test section which is 33" (0.84 m) and 91% of this length is heated. In order to minimize the axial heat conduction inside the cylinder, the end supports are thermally insulated from the cylinder. The cylinder can produce a maximum mean temperature rise of 0.8 °C at 53 diameters downstream from it and at free stream speed of 10.2 m/s.

The mandoline is used in different configurations to vary the ratio of the velocity integral length scale at the injection point to the scalar injection scale. Three parameters are studied: the width of the mandoline (w); the spacing between each wire (s); and the downstream position from the cylinder at which the mandoline is located (x_θ). The three parameters are shown in Figure 2.1.

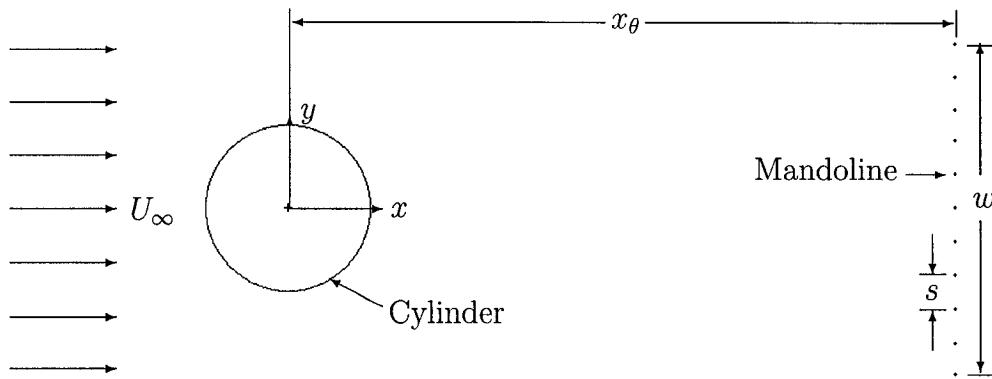


Figure 2.1: Physical parameters used to specify a mandoline configuration.

During the experiments, the wires reach a temperature around 250 °C, causing them to expand. To prevent the wires from sagging, small springs are attached to one of their ends, keeping them in tension irrespective of their temperature. The wires

are fixed in space using two end mounts that are electrically and thermally insulated by small ceramic plates. The mandoline is heated using a variable DC power supply rated at 75 V and 15 A maximum. The voltage out of the power supply is regulated to within 0.01%. To obtain the maximum signal to noise ratio, the mandoline is operated at maximum power. This power depends on the resistance of the mandoline which, in turn, depends on the number of wires used. The wires are connected in parallel such that adding wires reduces the total resistance of the mandoline. Because the number of wires used ranges from 6 to 17 (depending on w and s), two wire materials are used: nichrome (Type A) wires are used for mandolines composed of more than 15 wires; and stainless steel wires with enamel coating are used for the other mandolines. The diameter of the wires (d_{wire}) is kept constant at 0.005" (0.127 mm) since this offers an acceptable tensile strength and linear resistance, but is small enough to prevent the shedding of vortices ($Re_{d_w} = \frac{U}{\nu_{eff}} d_{wire} < 40$) and therefore have negligible influence on the flow. The influence of the mandoline on the flow will be discussed in more details in chapter 3.

2.3 Measurement Instruments

In this experiment, extensive velocity and temperature measurements are obtained using Hot-Wire Anemometry (HWA) in the Constant Temperature Anemometer (CTA) mode and Cold-Wire Thermometry (CWT) in the Constant Current Anemometer (CCA) mode, respectively. The CTA is an IFA-300 model made by TSI with two channels and the cold-wire thermometer was built at Université Laval. Each type of measurement requires a different sensor. For the velocity measurements, the wires are made of tungsten and have a diameter of 3.2 μm . Their resistance is around 5 Ω which corresponds to a length to diameter ratio of the order of 200.

For the temperature measurements, the cold-wires are made of platinum and have a diameter of 0.63 μm . The wire is made to have a resistance of about 180 Ω which corresponds to a length of 0.5 mm ($l_w/d \simeq 800$). This length to diameter ratio is lower than the value recommended by Browne and Antonia[49], who suggest that it should be around 1500 to minimize end losses and consequently the error on large-scale measurements. On the other hand, the aforementioned authors also say that the length of the wire should not be greater than five times the Kolmogorov scale (η) for spatial resolution reasons. In this flow, $l_w/\eta \simeq 4$ which is a good compromise between the two competing effects, given that both the large and small scales of the turbulence are of interest in this work.

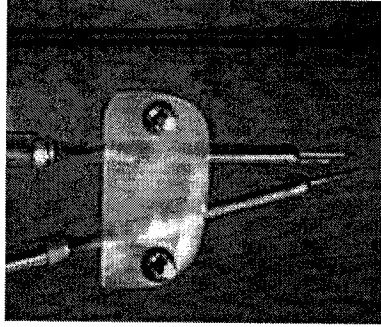


Figure 2.2: Velocity and temperature probe arrangement. The temperature probe is on the bottom.

The velocity field is measured using an X-wire probe to resolve two components of the velocity vector. When simultaneous velocity-temperature measurements are made, the temperature wire is mounted beside the X-wire. Its separation distance from the nearest hot-wire is 1 mm. This cannot be smaller due to the hot-wake of the velocity wire that could contaminate the temperature measurements. In order to prevent that, the temperature wire is also placed 0.25 mm upstream from the intersection of the X-wire probe. Figure 2.2 displays the velocity-temperature probe arrangement.

The velocity field was measured in two ways: With the X-wire alone and using the velocity-temperature probe holder. There are no significant differences in the velocity field indicating that the velocity-temperature probe holder has a negligible effect on the flow at the measurement point.

The mean flow velocity is verified using an 18" (0.48 m) straight pitot static tube with an external diameter of $\frac{1}{8}$ " (3.2 mm). The pressure difference was measured using an MKS Baratron type 220D pressure transducer with an accuracy of ± 0.01 Torr. The air density was computed assuming that the ideal gas law holds, measuring the temperature with a type E thermocouple and the absolute pressure using a standard mercury barometer. The pressure difference is transformed into a velocity using Bernoulli's equation:

$$U = \sqrt{\frac{2\Delta P}{\rho}}. \quad (2.1)$$

In some cases, transverse two-point temperature measurements are made using two cold-wire probes. One probe is held at a fixed location in the wake while the other probe is moved away from the fixed one using a traversing mechanism with a displacement accuracy of 0.02 mm. The two probes are aligned together in the z and

x directions and are separated by no more than 1 mm in the y (transverse) direction at the start of each experiment.

2.4 Calibration Procedures

The calibrations of the cold-wires and the hot-wires are different. Before performing any calibration, it is important that the material properties of the wires have stabilized. The hot-wires are operated at a temperature far above the room temperature. It is therefore important to operate any newly made hot-wire for at least 24 hours to allow for the material properties to reach a steady-state. This procedure is known as the *aging* or *burning* process of hot-wires. Aging is not needed for the cold-wires since they are operated at ambient temperature.

2.4.1 Cold-Wire Calibration

The current passing through the cold-wire is an important parameter to adjust before the calibration. If the current is too large, the wire will become “hot” and will be sensitive to velocity fluctuations. On the other hand, if it is too small, the output signal will be too small compared to the electronic noise. The current that is to be selected depends largely on the wire diameter. For a $0.63\ \mu\text{m}$ wire diameter, the recommended current is 0.1 mA[48]. In the present work, a current of 0.15 mA is used to improve the signal-to-noise ratio. At this slightly higher current, the sensitivity to velocity fluctuations in this flow remains negligible, as seen in Figure 2.3. The dashed line is the spectrum of the temperature for the case where the flow is not heated and therefore represents the background “thermal noise”. This background noise includes the noise caused by the sensitivity of the cold-wire to velocity fluctuations, the electronic noise, and the noise caused by ambient temperature fluctuations. The series of spikes (at discrete frequencies) that appears in this spectrum is attributed to AC electrical noise because the spikes occur at frequencies of 60, 120 and 180 Hz. This spectrum is several orders of magnitude smaller than the one for the heated wake (shown as the solid line) and of non-turbulent nature indicating that the wire sensitivity to velocity fluctuations is negligible.

The cold-wires are calibrated in a circular laminar jet. The velocity of the jet is chosen to be close to the mean velocity of the experiment and is held constant over the whole calibration. The air passing through the calibration jet is heated using 3 120 W electric heaters that are attached on the outside of a 2” (50.8 mm) copper pipe

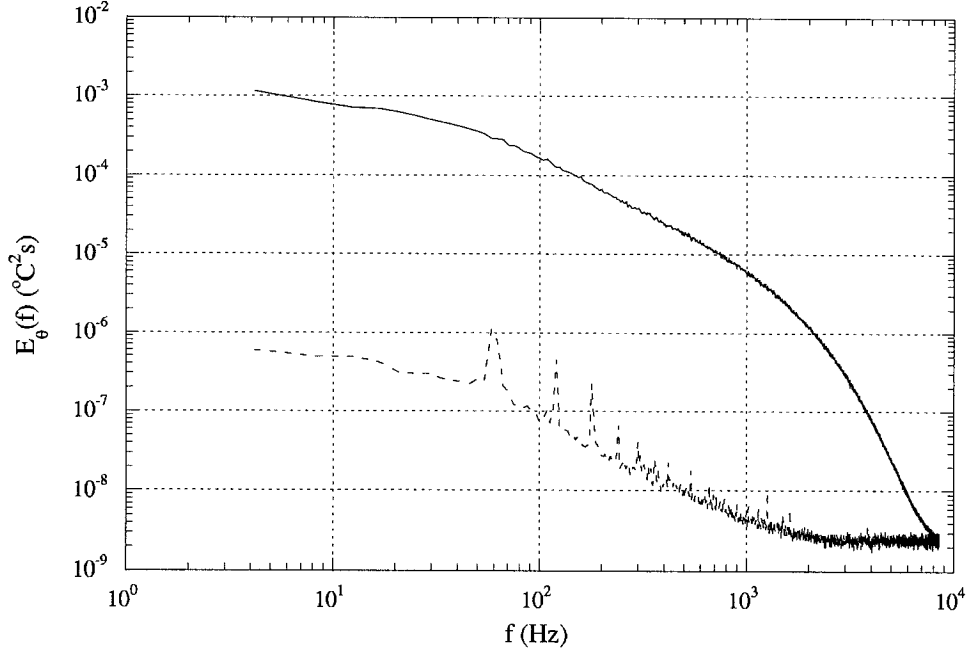


Figure 2.3: Power spectral density of the temperature field. Solid line: heated wake, dashed line: isothermal wake.

connected to the air supply. The supply line is carefully insulated so that no irregular fluctuations in jet temperature occur during the calibration. The temperature of the jet is measured to an accuracy of 0.1 °C using a type-E thermocouple connected to a digital display. Once the jet is heated to a high temperature (around 45 °C), it is allowed to cool down, and after a certain amount of time the temperature of the jet decreases monotonically. From that time, the calibration may begin. Twelve to fifteen points are taken over a range of at least 5 °C. A typical calibration curve is shown in Figure 2.4.

The relationship between the temperature and the cold-wire thermometer output voltage is clearly linear. Choosing a material whose resistance changes linearly with temperature permits one to express the temperature as a (linear) function of the voltage: $T = A \times E + B$. A least-square fit to the calibration points is used to obtain the sensitivity (A) of the wire. A theoretical expression for A can also be obtained[48]:

$$A = \frac{1}{Gi\beta R_o} \quad (2.2)$$

where β is the coefficient of thermal resistivity of the wire material ($\beta = 0.0039 \Omega/\Omega^\circ\text{C}$ for platinum), i is the current passing through the wire, G is the circuit gain, and R_o is the resistance of the wire at room temperature. The circuit gain can be computed by producing a known change in resistance of the sensor. This can be accomplished

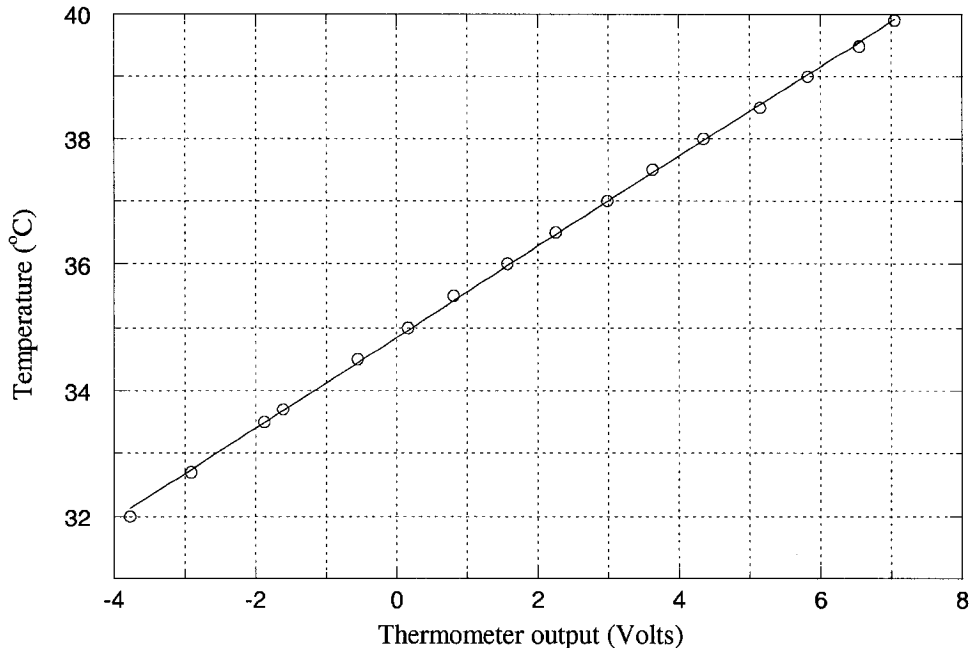


Figure 2.4: Calibration curve for a cold-wire.

using a simple electronic circuit. Following Ohm's Law: $\Delta E = Gi\Delta R$, and given that the current is constant, the gain G can be deduced. It is therefore possible to compare the experimental result for A to the theoretical one. For all the cold-wires used here, the experimental values are within 2.5% of the theoretical ones. The experimental value of A was used in the data analysis.

The gain was also changed from the calibration to the experiment in order to best fit the signal to the range of the A/D board (to be discussed in §2.5). The new sensitivity is computed using Eq. (2.3), which is deduced from Eq. (2.2)

$$A_{exp} = A_{cal} \frac{G_{exp}}{G_{cal}}. \quad (2.3)$$

The offset B in the linear relationship is needed to obtain the absolute temperature. It was computed every day by placing a type-E thermocouple in the free stream of the wind tunnel and recording the corresponding CCA output voltage.

The cold-wire also possesses a natural (thermal) frequency, called the cut-off frequency (f_c). If f_c is significantly smaller than the Kolmogorov frequency, experimental error (in the form of poor temporal resolution) will occur. f_c is also a good indication of the state of the cold-wire. If its frequency response is slow, it is because something prevents the wire from changing its temperature. It may be dust on the wire (fouling) or some coating that has not been removed during the etching process

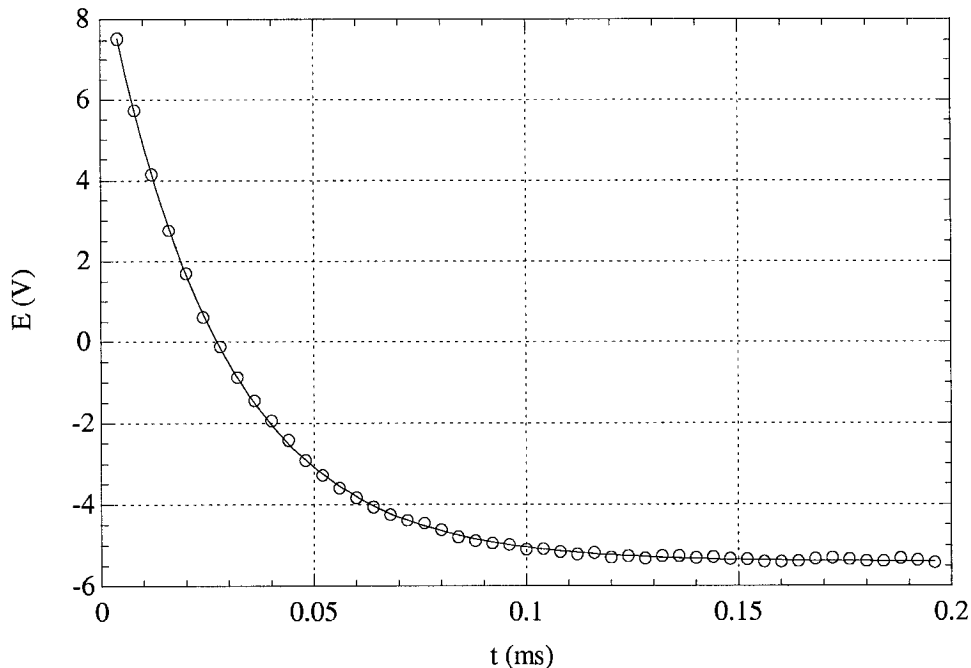


Figure 2.5: Response of a cold-wire to the current injection technique.

of a new wire. Following the current injection technique proposed by Lemay and Benaïssa[50], the cold-wire time constant can be measured before each calibration and each experiment. A typical wire response to the square wave current injection is shown in Figure 2.5.

The cut-off frequency of all the cold-wires is computed by performing a least-square fit on the data using the following equation:

$$E = Ae^{-t/\tau_e} + Be^{-t/\tau_w} + C. \quad (2.4)$$

This equation was proposed by Lemay and Benaïssa[50]. The time constant of the electronics used here is $\tau_e = 3 \mu\text{s}$. In general, the results for f_c ($f_c \equiv 1/(2\pi\tau_w)$) are lower than the theoretically predicted values when using a wire diameter of $0.63 \mu\text{m}$. A likely reason for this is that the actual diameter is bigger than the value specified by the manufacturer.

2.4.2 Hot-Wire Calibration

The calibration of a hot-wire is more complicated. The anemometer response to flow velocities is non-linear. Some researchers use a third order polynomial to account for this non-linearity. Here, a modified King's Law (Eq. 2.5) is used because it is derived from basic heat transfer principles:

$$E^2 = AU^n + B. \quad (2.5)$$

Eq. (2.5) is applicable to isothermal flows. In the present case, however, the flow is not isothermal. In order to account for the temperature fluctuations, Lienhard[51] proposed corrections for A and B based on heat transfer principles and on the empirical effect of the temperature on fluid properties:

$$A = \bar{A} \left(\frac{T_\infty + T_{w,a}}{2} \right)^{0.84} (T_{w,a} - T_\infty) \quad (2.6)$$

$$B = \bar{B}(T_{w,b} - T_\infty). \quad (2.7)$$

T_∞ is the flow temperature and is known from the cold wire measurement. The other parameters (\bar{A} , \bar{B} , $T_{w,a}$, and $T_{w,b}$) need to be determined by calibration. $T_{w,a}$ and $T_{w,b}$ both represent the temperature of the hot-wire, but are not forced to be the same. One way to determine the four parameters is to vary the jet velocity for different jet temperatures. This calibration is not a trivial task since the heat transfer to the air depends on the flow rate through the electric heaters. In order to accomplish this, a 0.5 m³ reservoir is hooked up to the supply line of the calibration jet. The reservoir's thermal inertia damps out any fluctuations in temperature when the jet velocity is varied. Even using the reservoir, the velocity range at which the wire is to be calibrated also slightly influences the temperature of the jet. Consequently, the velocity range was chosen to be from 5 to 18 m/s, which corresponds to approximately four standard deviations from the mean velocity of the present experiment. For this velocity range, the variation in jet temperature for one velocity calibration is between ± 0.1 and ± 0.2 °C. An example of this calibration for one channel of an X-wire is shown in Figure 2.6.

The need to account for temperature variations is clearly demonstrated in Figure 2.6. Equation (2.5) is used to perform a least-square fit to all five velocity curves. The exponent n is approximately temperature independent and is therefore set constant for all curves. A set of A and B coefficients is then obtained. These are used with the corresponding temperatures (T_∞) to determine \bar{A} , \bar{B} , $T_{w,a}$, and $T_{w,b}$ in equations (2.6) and (2.7), again by a least-square fit.

In order to determine the u and v components of velocity, the X-wire must also undergo a yaw-calibration. The yaw-angle calibration is done using the effective angle method proposed by Browne *et al.*[52]. The X-wire is calibrated over 8 different yaw

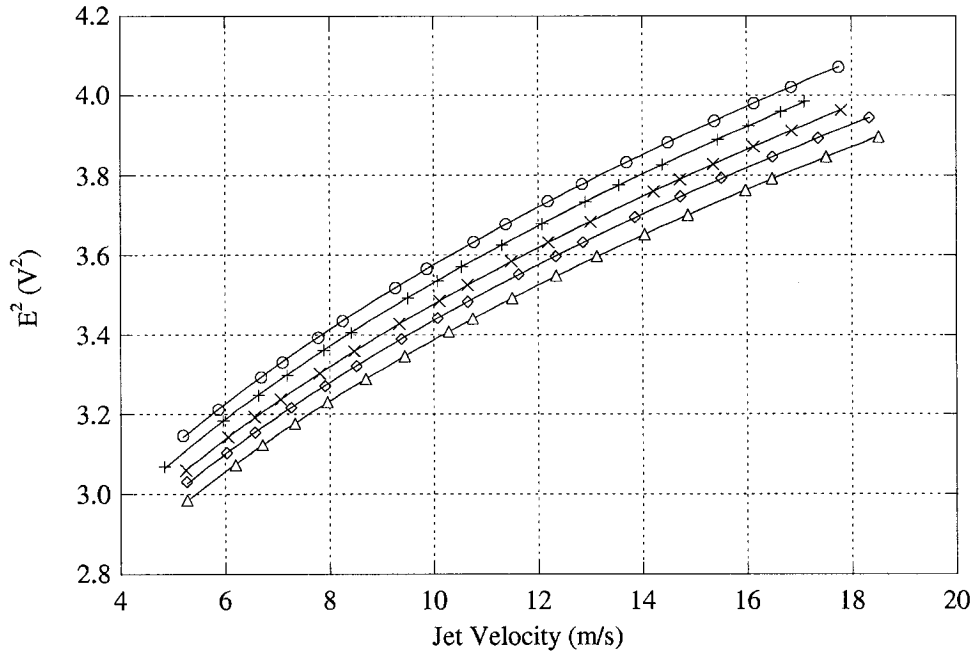


Figure 2.6: Calibration curves for a hot-wire at different flow temperature.
 \circ : $T = 22.5$ °C, $+$: $T = 27.5$ °C, \times : $T = 31.4$ °C, \diamond : $T = 34.5$ °C, \triangle : $T = 37.7$ °C.

angles ranging from -24° to 24° in 6° increments. Because the two hot-wires are not perpendicular to the flow, they will be cooled by the cross-flow and the flow parallel to them. As suggested by Browne *et al.*, the ratio of the two cooling modes (k) is set constant (independent of the orientation of the wire to the flow). Here, the value of 0.03 for k^2 , as recommended by Browne *et al.*, is used. The effective angle is then taken as the average of the 8 corresponding yaw angle results. Usually, the maximum variation in effective angle for the different yaw angles is $\pm 1.5^\circ$. The yaw calibration is assumed to be independent of the flow temperature. This assumption is verified for two different temperatures and the difference in the effective angles is within 1° . Table 2.1 displays typical calibration results for the two channels of the X-wire:

Anemometer Channel	1	2
n	0.44	0.44
$\bar{A}(\times 10^5)$	5.46	5.49
$\bar{B}(\times 10^3)$	2.11	2.05
$T_{w,a}$	514.5	510.5
$T_{w,b}$	594	589
θ_{eff}	46.8	50.3

Table 2.1: Typical calibration constants for the two channels of an X-wire.

The frequency response of hot-wires is faster than that of cold-wires because

the temperature difference between the hot-wire and the flow is larger. In the CTA manual, it is stated that the hot-wires have a frequency response of 260 kHz for a 3.8 μm diameter tungsten wire and a flow velocity of 100 m/s. It is therefore not necessary to compute their cutoff frequency because the maximum frequency encountered in the present flow is approximately 10 kHz.

2.5 Data Acquisition and Analysis

The signals from the CTA and the CCA are connected to a Kron-Hite model 3384 band-pass filter for low- and high-pass filtering. They are then connected to a National Instrument PC-MIO-16E-4 DAQ (Data Acquisition) board. The DAQ board is controlled using LabVIEW5.0. The probes are moved across the wake using a home-made traversing mechanism that is also controlled using LabVIEW. The low- and high-pass frequencies are determined using a Virtual Instrument (VI: LabVIEW program) that computes the power spectral density of the electronic signal. The low-pass frequency is set to the local minimum in the high frequency range of the dissipation spectrum. This local minimum, when the electronic noise is small, is on the order of the Kolmogorov frequency. The high-pass frequency is set at the local minimum of the power spectral density multiplied by the frequency ($f \times E(f)$) (generally 0.05 Hz).

The same VI also displays the voltage range coming from the filter of each channel. The gain of the DAQ board is adjusted such that the signal covers between 50% and 80% of the input range. The gain on the CTA is adjusted to have approximately the same voltage range as the temperature signal, because the gain of the DAQ board should be the same for the three channels as time delays would occur if the DAQ were to change its gain between channels. The data acquisition has a resolution of 12 bits such that each bits represent 0.024% of the data range.

Both components of velocity and temperature are taken quasi-simultaneously. The DAQ board has a minimum inter-channel delay of $4\mu\text{s}$. The data can be assumed to be taken simultaneously since this time lag is only 4% of the smallest time scale in the flow.

Two types of data files are recorded for every point. One type is used to compute large-scale statistics of the flow such as the root mean square value, the skewness and kurtosis or the turbulent heat fluxes. For this type of data, each sample needs to be independent from the previous one. The samples become independent if the time that separates them is greater than the integral time scale. In this experiment, the

integral time scale is smaller than 0.005 sec such that these data were taken at 200 Hz. 10 blocks of 4096 samples are recorded for each position except at the centreline where 100 blocks are taken for a total record-length of 34 minutes.

The other type of data is used to compute spectra, auto-correlations, or structure functions such that a complete time series is required. For this type of data file, the sampling frequency is twice the low-pass filter frequency to avoid aliasing. 100 blocks of 4096 samples are taken at each position except at the centreline where 1000 blocks are recorded for the improved convergence of higher-order statistics. In addition, to resolve the low frequency part of the power spectra, 1000 blocks of 4096 samples are also taken at 1 kHz (about ten times slower than the Kolmogorov frequency) at the centreline only. For this last data file, the low-pass frequency is half the sampling frequency (500 Hz).

The temperature signal for the time series is also corrected for the frequency response of the cold wire before being analyzed. This is done in FORTRAN90 by computing the Fourier transform of each block of data, applying a filter function to it, and then computing the inverse Fourier transform. The filter function that is used is the one suggested by Lemay and Benaïssa[50]:

$$H_f(f) = |H_f(f)| \exp(-i\phi(f)) \quad (2.8)$$

with

$$|H_f(f)| = \sqrt{\frac{1 + (f/f_c)^2}{1 + (f/f_K)^4}} \quad (2.9)$$

and

$$\phi(f) = -\arctan(f/f_w) \quad (2.10)$$

where f_c is the cut-off frequency of the wire and its measurement was discussed earlier; f_K is the low-pass frequency. Using this correction, the dissipation increases by at least 20% and the small-scale collapse in the power spectral density improves. To give an idea of the importance of the frequency response correction, the scalar dissipation spectra of the same signal, one is not compensated while the other is compensated, is shown in Figure 2.7.

The data is processed using a numerical program that was revised and translated to FORTRAN90 by Sébastien Beaulac in 1999.

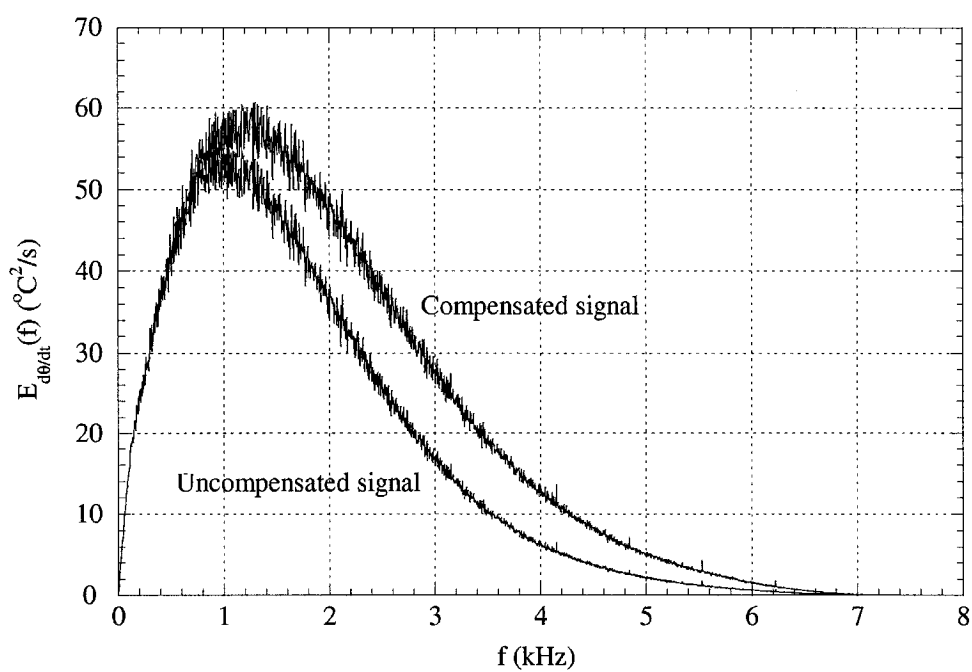


Figure 2.7: Effect of the frequency correction on the dissipation spectra.

Chapter 3

Flow Field

In this chapter, the flow field characteristics will be described. The symmetry of the wake will be discussed, and the independence of the turbulence statistics in the direction parallel to the cylinder axis will be verified. A discussion of the perturbation of the flow by the mandoline will follow, and a proof of the passivity of the scalar will be made. Then the temperature field will be validated for the heated cylinder.

3.1 Velocity

All the experiments were conducted at the same free stream velocity, U_∞ , of 10.2 m/s. This results in a Reynolds number based on the cylinder diameter of 16.2×10^3 . At this flow velocity, the Root Mean Square (RMS) of longitudinal velocity fluctuations ($u_{RMS} = \langle u^2 \rangle^{\frac{1}{2}}$) is 0.61 m/s at the centreline and a downstream position of 53 diameters which results in a turbulence intensity of 6%. This low turbulence intensity indicates that Taylor's frozen flow hypothesis should be applicable throughout. The RMS of the transverse velocity components is 0.53 m/s. The *skewness* ($S_u = \langle u^3 \rangle / \langle u^2 \rangle^{\frac{3}{2}}$) of both components of velocity is always smaller than 0.06 at the centreline and the *flatness* or *Kurtosis* ($F_u = \langle u^4 \rangle / \langle u^2 \rangle^2$) is around 2.86 for each velocity components. Table 3.1 displays the most important turbulent scales at two downstream positions.

x/D	53	89
ℓ (mm)	40	57
λ (mm)	3.8	5.2
η (mm)	0.15	0.21

Table 3.1: Principal velocity length scales of the flow at $Re_D = 16.2 \times 10^3$.

All the length scales in Table 3.1 are longitudinal in nature. ℓ is the integral scale, λ is the Taylor microscale and η is the Kolmogorov scale of the velocity fluctuations. The integral scale is obtained by evaluating the integral of the auto-correlation function up to its first zero (as suggested by Comte-Bellot and Corrsin[54]). The temperature integral length scale will be evaluated in the same way. λ and η are computed using formulae proposed in Tennekes and Lumley[9]:

$$\lambda = \langle U \rangle \sqrt{\frac{\langle u^2 \rangle}{\langle \left(\frac{\partial u}{\partial t}\right)^2 \rangle}} \quad (3.1)$$

and

$$\eta = \left(\frac{\nu^3}{\epsilon}\right)^{1/4}. \quad (3.2)$$

The value of the dissipation rate of turbulent kinetic energy is required to compute η . It is obtained assuming small-scale isotropy and Taylor's frozen flow hypothesis:

$$\epsilon = \frac{15\nu}{\langle U \rangle^2} \left\langle \left(\frac{\partial u}{\partial t}\right)^2 \right\rangle. \quad (3.3)$$

3.1.1 Structure of the Hydrodynamic Wake

It is of interest to look at the symmetry of the wake. Since the imposed geometry is symmetric about the x-z plane, turbulent statistics should also be symmetric about this plane. Figure 3.1 suggests that the mean longitudinal velocity ($\langle U \rangle$) is symmetric. A least-square fit of the form $\langle U \rangle = A - B \exp\left(\frac{-(y-y_o)^2}{h^2}\right)$ was performed on the data. Since the cylinder is placed at the middle of the tunnel, the origin for y is also chosen to be the middle of the tunnel. The value of the offset y_o in the curve fit is $0.02D$. The value of h, the half-width of the wake at this downstream location is 2.85 diameters. The present value is lower than the one obtained by Kang and Meneveau[37] ($Re_D = 4.1 \times 10^4$) and is higher than the one obtained by Matsumura and Antonia[36] ($Re_D = 5.83 \times 10^3$). The centreline velocity (U_c) is 8.9 m/s such that $U_c/U_\infty = 0.86$ which is very close to the values obtained by Matsumura and Antonia.

In Figure 3.2 the RMS profile of the velocity fluctuations displays a larger asymmetry. The peak of u_{RMS} is higher for $y < 0$. However, the axis of symmetry of both profiles remains close to $y = 0$.

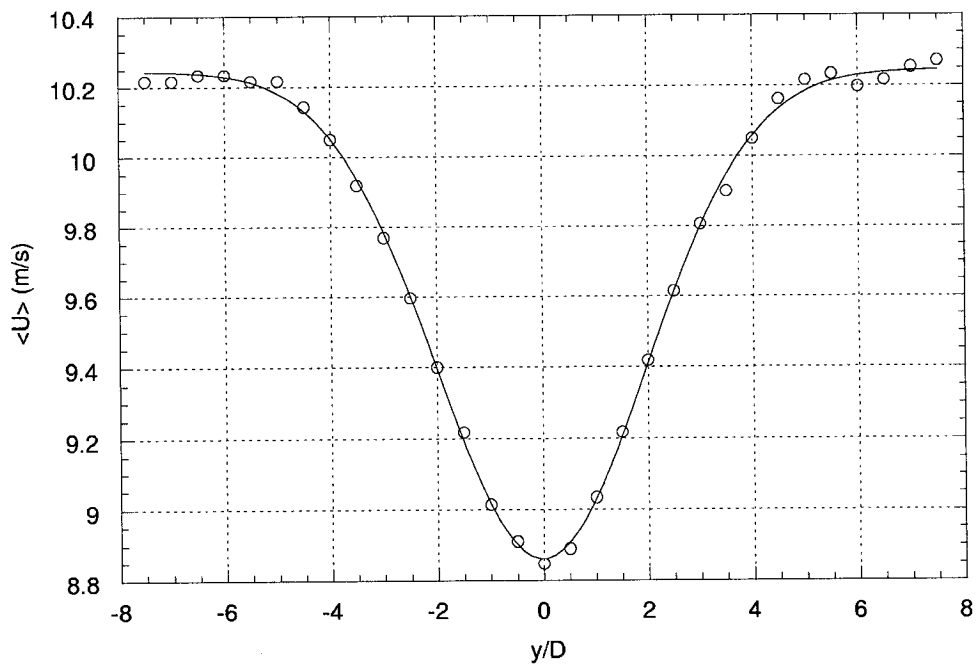


Figure 3.1: Longitudinal mean velocity profile. $x/D = 53$.

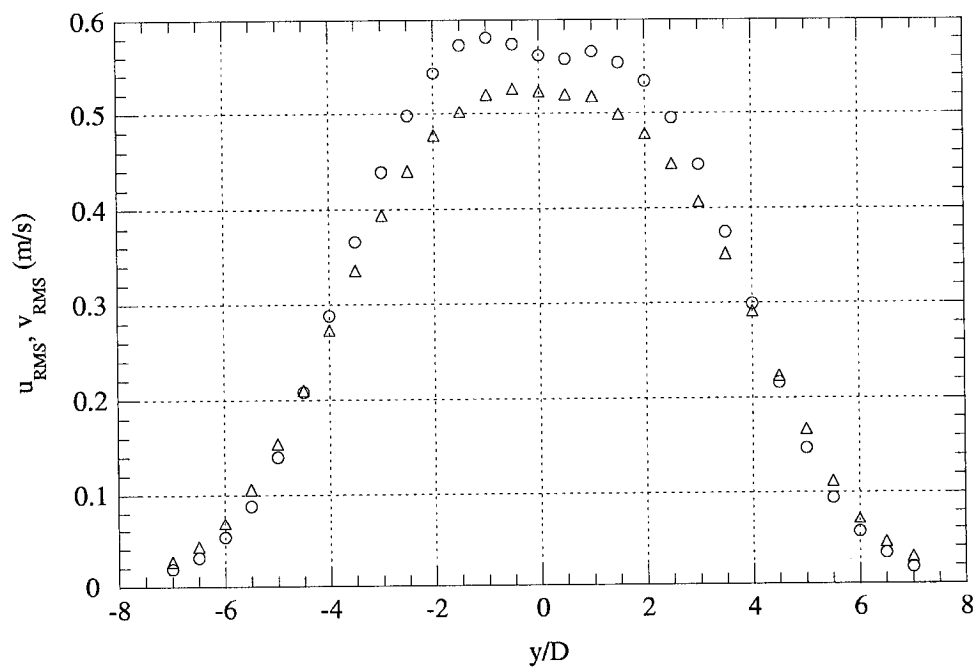


Figure 3.2: RMS of the velocity fluctuations. ($x/D = 53$). \circ : u , \triangle : v .

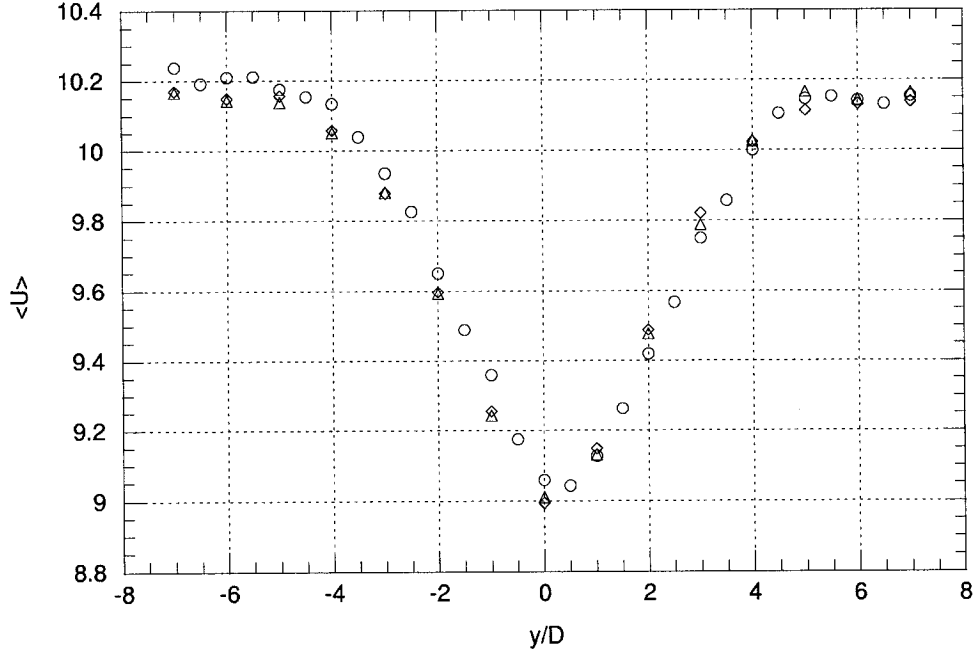


Figure 3.3: Mean velocity profile for different heights. ($x/D = 53$). \circ : $z/D = 0$, \triangle : $z/D = -2$, \diamond : $z/D = -3.5$.

Another geometrical property of the wake of a long cylinder ($L \gg D$) is that, far enough from the cylinder ends, statistics should not vary in the direction parallel to the cylinder axis. In this experiment, the length to diameter ratio of the cylinder is 34 which should be enough to guarantee a two-dimensional region. In order to verify if such a two-dimensional region exists, a series of measurements are made at planes below the mid-plane, namely $z/D = -2$ and $z/D = -3.5$. Figures 3.3 and 3.4 show that the mean velocity profile and the RMS of v and u (not shown) are hardly affected by the height.

The power spectral density of u is shown in Figure 3.5 for three locations along the axis: clearly, the structure is independent of the height. From Figures 3.3, 3.4, and 3.5, it appears that the flow is two-dimensional for a central portion of at least 7 diameters.

3.1.2 Influence of the Mandoline on the Flow

The purpose of a mandoline is to be able to inject the scalar at different scales without disturbing the velocity field. This is, however, ideal and the mandoline may influence the flow.

The mandoline wire diameter ($d_{wire} = 0.127$ mm) is chosen small enough to avoid

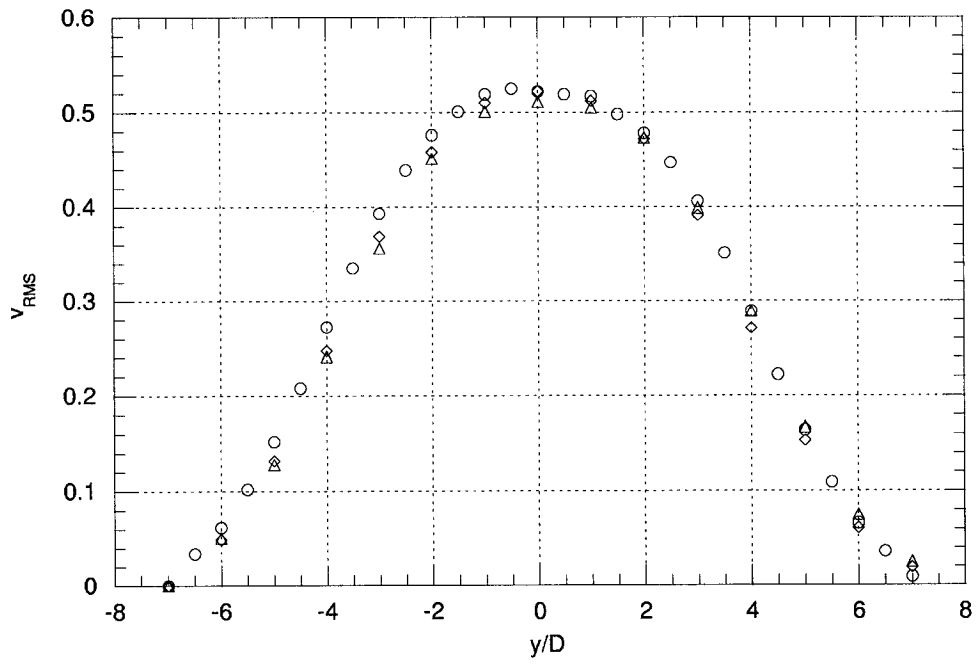


Figure 3.4: RMS profile of v for different heights. ($x/D = 53$). \circ : $z/D = 0$, \triangle : $z/D = -2$, \diamond : $z/D = -3.5$.

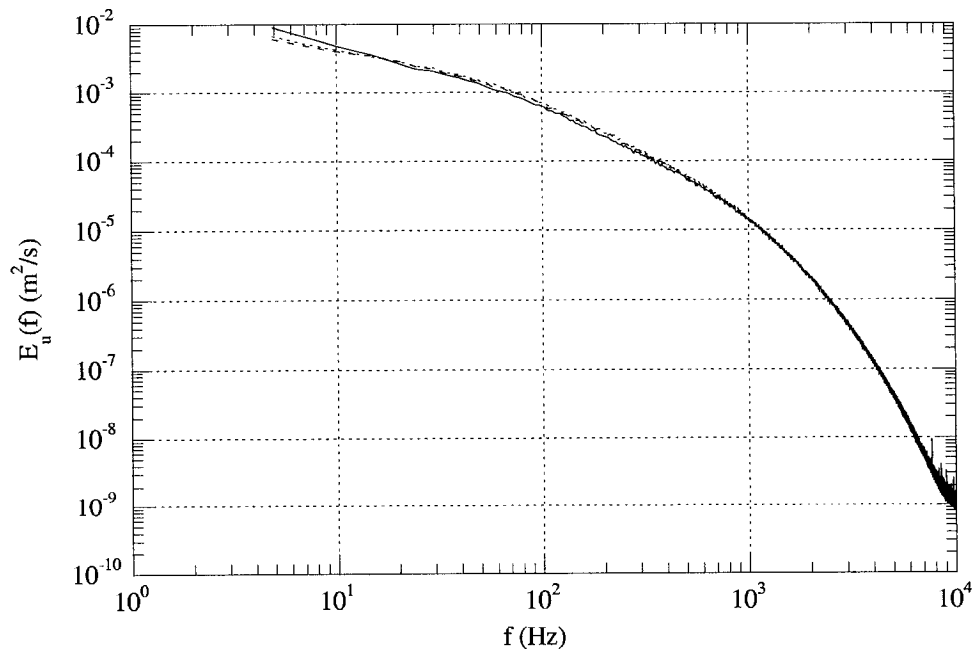


Figure 3.5: Power spectral density of u for different heights. ($x/D = 53$ and $y/D = 0$).

the shedding of vortices as discussed in Chapter 2. This is true, however, only when the wires are hot, because of the increase in the film temperature. For $s/D = 0.1$, the flow blockage is 5.5 %. The velocity field along the centreline at $x/D = 53$ was measured for the following four conditions:

1. Empty tunnel.
2. Mandoline only.
3. Cylinder only.
4. Cylinder and mandoline.

The mandoline was not heated. Therefore, its effect on the velocity field will be overestimated given that the Reynolds number using a film temperature will be larger than what it is during the experiments. The mandoline causes the background turbulence intensity to increase slightly from 0.12% to the (still low) value of 0.17%. When placed in the wake of the cylinder, the mandoline causes a measurable increase in u_{RMS} (from 0.58 m/s for the cylinder only to 0.61 m/s with the mandoline), but S_u and F_u remain unchanged. The power spectral density shown in Figure 3.6 indicates that the mandoline affects the large scales primarily. The mandoline has negligible effect on the lateral component of velocity.

The reason why the influence of the mandoline on the flow is greater when the cylinder is present could be attributed to excitation of the wires by the von Kármán vortex street. If the frequency at which the von Kármán vortices are being shed (f_v) is close to the natural frequency of the mandoline wires (f_m), the wires could start to vibrate and disturb the flow. It is therefore important to estimate the natural frequency of the mandoline wires and make sure that $f_m \gg f_v$.

The mandoline wires behave like vibrating strings with their fixed ends located at the junction to the springs. Therefore their resonance frequencies are given by:

$$f_{res} = \frac{n\pi}{L} \sqrt{\frac{T}{\sigma}} \quad (3.4)$$

where σ is the mass per unit length (Kg/m) of the wires, T is the tension in the wires, and L is their length. The fundamental natural frequency of the wires is obtained by setting $n = 1$. By expressing σ in terms of the density, ρ_w , and the wire diameter, d_w , the following formula is obtained:

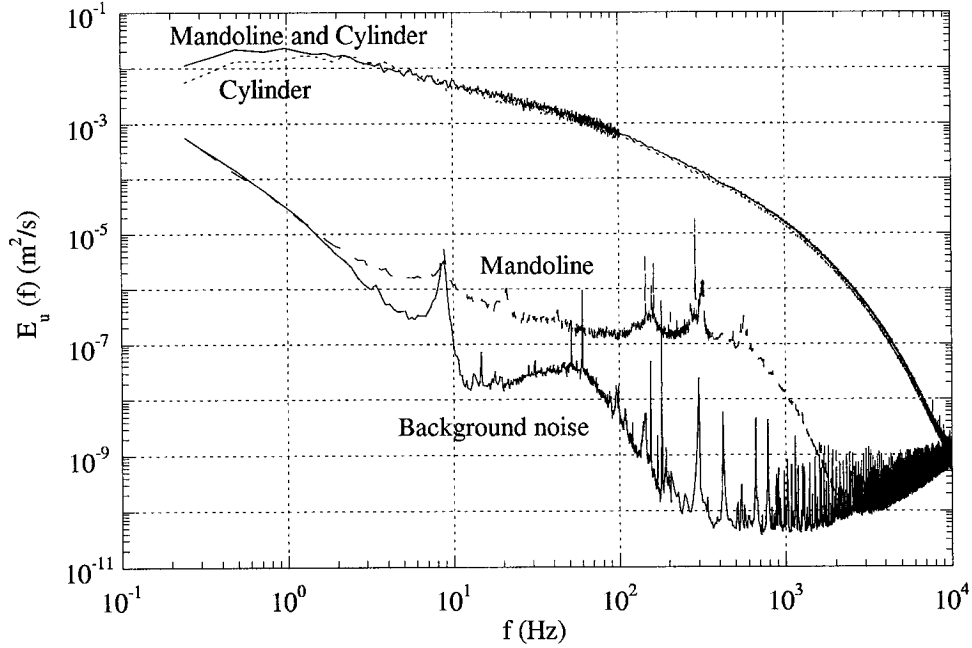


Figure 3.6: Effect of the mandoline on the power spectral density of u .

$$f_m = \frac{2}{Ld_w} \sqrt{\frac{T\pi}{\rho_w}}. \quad (3.5)$$

For stainless steel, $\rho = 7930 \text{ Kg/m}^3$ and for nichrome, $\rho = 8430 \text{ Kg/m}^3$. The wire diameter is 0.127 mm and their length is $0.70 \pm 0.01 \text{ m}$. The most difficult parameter to estimate is the tension in the wires because the length of the springs was not constant, therefore affecting the spring constant and they were not stretched by the same amount. The average spring constant (k) is estimated to be around 150 N/m and their average extension is 30 mm. (This results in a tension of 4.5 N which corresponds to a tensile stress of 350 MPa. This is lower than, but close to the yield stress for both, nichrome and stainless steel. As expected since some wires suffered from permanent plastic deformations when installed.) f_m is then estimated to a value of 1 KHz.

For $Re_D = 16.2 \times 10^3$, the Strouhal number ($S_t = f_v D / U_\infty$) is approximately constant and equal to 0.21. It is therefore straightforward to obtain the frequency of the vortices ($f_v \approx 85 \text{ Hz}$). It is thus, very unlikely that the von Kármán vortex street will cause the mandoline wires to oscillate.

Some influence of the mandoline on the flow field is to be expected. Numerous studies of velocity perturbations in grid-generated turbulence have been conducted. Townsend[55] describes the effect of wire gauzes on turbulence as a net damping effect.

This effect is observed in grid-generating turbulence even if the wire diameter of the screen is too small to shed vortices and even if the screen has very low solidity. For example, in Sreenivasan *et al.*[46], it was observed that the heating screen changes the decay rate of the velocity fluctuations.

In this case, although the mandoline only causes a slight increase in the background turbulence when it is placed alone in the tunnel, its small perturbation to the velocity field seems unavoidable.

3.1.3 Effect of the Scalar

This work treats the mixing of passive scalars. “Passive” implies that the scalar does not affect the flow field. Here, the scalar is temperature, and since the density of air is inversely proportional to its temperature (for incompressible flows), the scalar cannot be passive in the presence of a gravity field. However, if the buoyancy force created by the temperature fluctuations is small compared to other forces acting at the same scale, the effect of the scalar on the flow field can be neglected and the scalar can be treated as passive.

There are several ways to determine whether the temperature can be treated as passive. Two will be used here. The first one will be to compare some turbulent statistics of velocity for the isothermal case and the heated case. The second one will be to compare the ratio of the buoyancy forces to the inertial forces in the flow. For the case of the isothermal flow, neither the cylinder nor the mandoline heats the flow.

Buoyancy can affect any scale in the flow. Table 3.2 illustrates the most important flow statistics for the isothermal wake and the wake heated by the cylinder.

	Isothermal wake	Heated Wake
u_{RMS} (m/s)	0.62	0.61
ℓ (mm)	40.3	40.0
λ (mm)	3.79	3.73
η (mm)	0.154	0.154
ϵ (m ² /s ³)	7.21	7.24
S_u	0.048	0.048
F_u	2.87	2.86

Table 3.2: Effect of the temperature on the important velocity length scales.

The differences in Table 3.2 are within experimental error. To examine the effect of the temperature on every scale in the velocity field, the power spectral density is

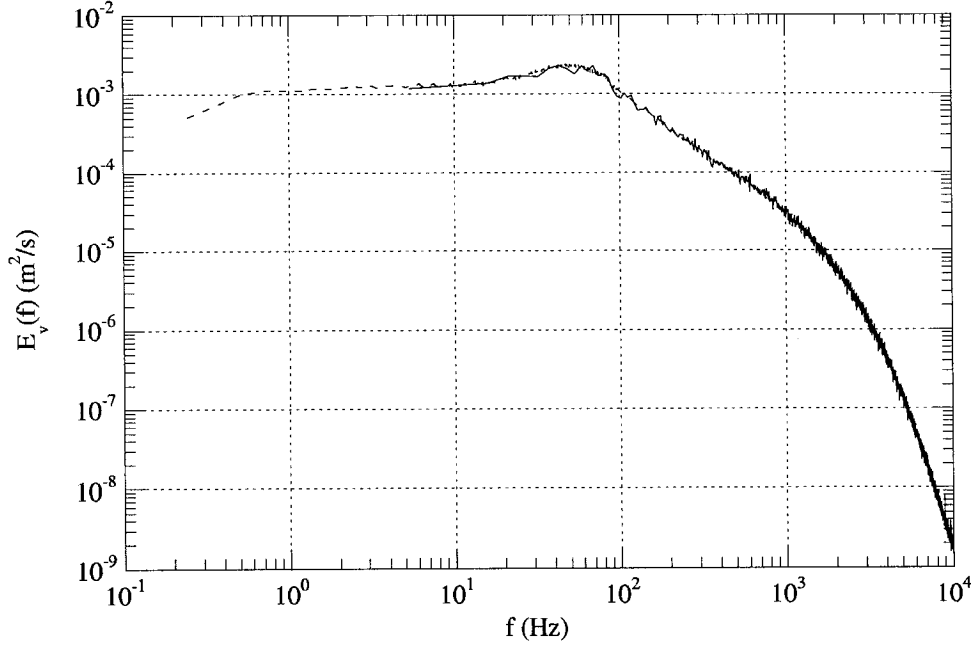


Figure 3.7: Effect of the temperature on the power spectral density of v . solid line: Isothermal wake, dashed line: Heated wake.

used. In Figure 3.7, the spectrum of v (the velocity fluctuation in the direction of the largest temperature gradient) shows no discernable effect.

The importance of the buoyancy force compared to the inertial force can be measured using the Bolgiano length scale (L_b). The Bolgiano length scale is computed by equating two turn-over times. The first one is the time for the energy of the flow to transfer from an eddy to a smaller one due to buoyancy effects. The second is the same time for inertial forces. Consequently, if the Bolgiano length scale is larger than the integral length scale, it means that temperature fluctuations are too small to have the time to cause an energy transfer in the velocity eddies. The Bolgiano length scale is defined as follow:

$$L_b = \frac{\epsilon^{5/4}}{\epsilon_\theta^{3/4}(\phi g)^{3/2}} \quad (3.6)$$

where ϕ is the volumetric thermal expansion coefficient ($\phi = \frac{1}{v} \left(\frac{\partial v}{\partial T} \right)_P = 3.4 \times 10^{-3} \text{ K}^{-1}$ for air under the experimental conditions) and g is the gravitational acceleration ($g = 9.81 \text{ m/s}^2$). For the Bolgiano scale to be small, either ϵ has to be small or ϵ_θ has to be large. In this flow, ϵ is fixed so that the only parameter is ϵ_θ . The Bolgiano scale is closest to ℓ at $x/D = 89$. At this downstream position, $L_b = 2.6 \times 10^3 \text{ m}$ for the cylinder and $2.4 \times 10^3 \text{ m}$ for the mandoline with the highest ϵ_θ . For both of these

cases, $L_b \gg \ell$ which indicates that the temperature is indeed a passive scalar.

3.2 Temperature

The heated cylinder generates a mean temperature rise of 0.8 °C at the centreline and a downstream position of 53 diameters for the above-mentioned flow velocity. This mean temperature excess results in a RMS value for the temperature fluctuations (θ_{RMS}) of 0.23 °C. The skewness and flatness factors go from -0.08 and 3.00 at $x/D = 53$ to -0.22 and 3.05 at $x/D = 89$. The value of F_θ agrees very well with Figure 1 of Mi and Antonia[39]. The skewness cannot be compared directly since it is a function of Re_D . In Figure 1 of Mi and Antonia, the downstream evolution of S_θ is measured for a slightly lower Reynolds number ($Re_D = 1.2 \times 10^3$) so that the present value of S_θ cannot be compared directly with this graph. However, Figure 4 of Mi and Antonia indicates that S_θ should be negative after $x/D \simeq 42$ for $Re_D = 16.2 \times 10^3$. The present results for S_θ therefore agree well with the results of Mi and Antonia.

3.2.1 Structure of the Thermal Wake

Like for velocity, the thermal field should be symmetric. Even if the velocity field is symmetric, other factors (e.g., background temperature gradient) could cause the temperature field to be asymmetric. The mean temperature excess ($\langle T \rangle - T_\infty$) profile is shown in Figure 3.8. Similarly to the mean velocity profile, a Gaussian least-square fit is performed on the data. The mean temperature excess is not as well represented by a Gaussian profile as the mean velocity. However, the profile is highly symmetric. Again, the origin for y is taken as the center of the tunnel and the offset value y_o from the Gaussian curve fit is small ($y_o/D = -0.2$). The value for the thermal half-width (h_θ) is 3.9 diameters. This value is larger than h , in agreement with previous results[45, 53].

The RMS profile of the temperature fluctuations is shown in Figure 3.9. Unlike the RMS velocity profile, the RMS temperature profile is close to symmetric.

In section 3.1, the velocity field was shown to be two-dimensional. If the scalar is injected uniformly along the cylinder, its field should also be two-dimensional. There are a number of factors that could create some temperature gradients along the cylinder axis. The cylinder ends are insulated to reduce the axial heat transfer and the tubular heater occupies 91% of the cylinder length so that the injection of heat should be uniform in the central part of the wake.

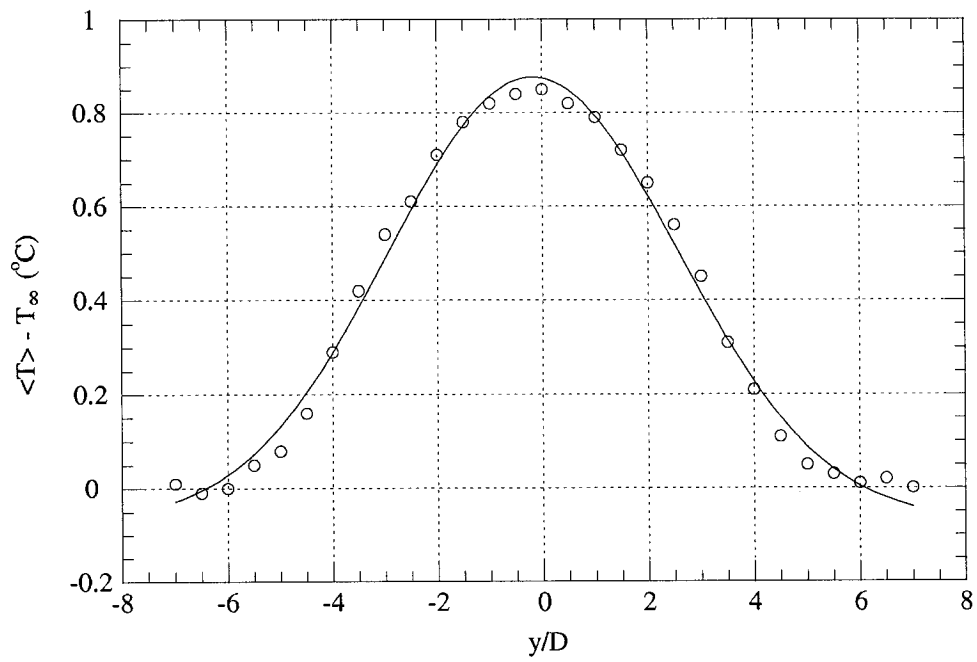


Figure 3.8: Mean temperature excess profile. ($x/D = 53$)

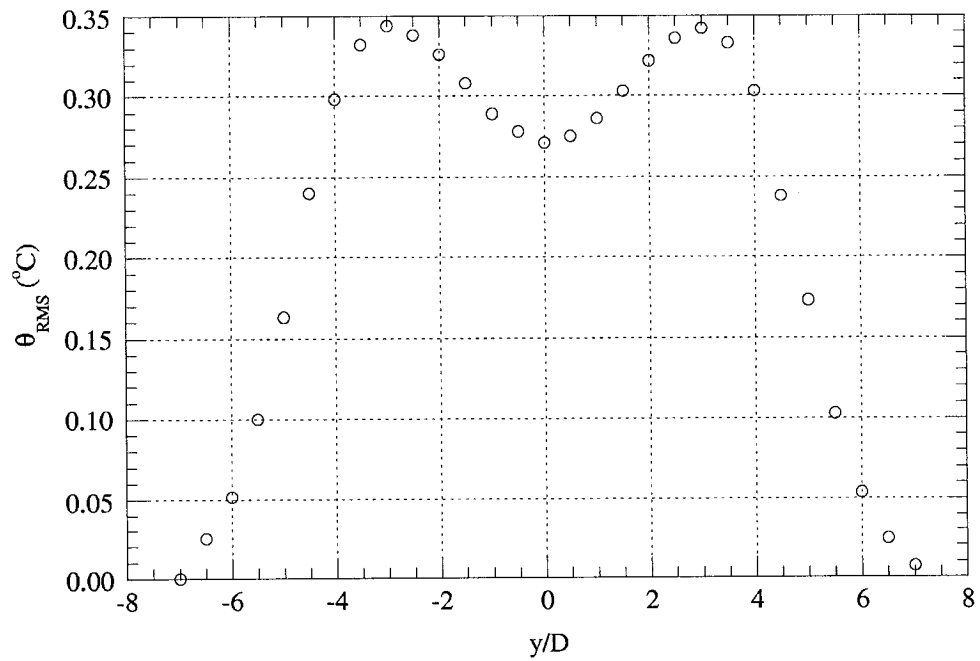


Figure 3.9: Profile of the RMS of temperature fluctuations. ($x/D = 53$)

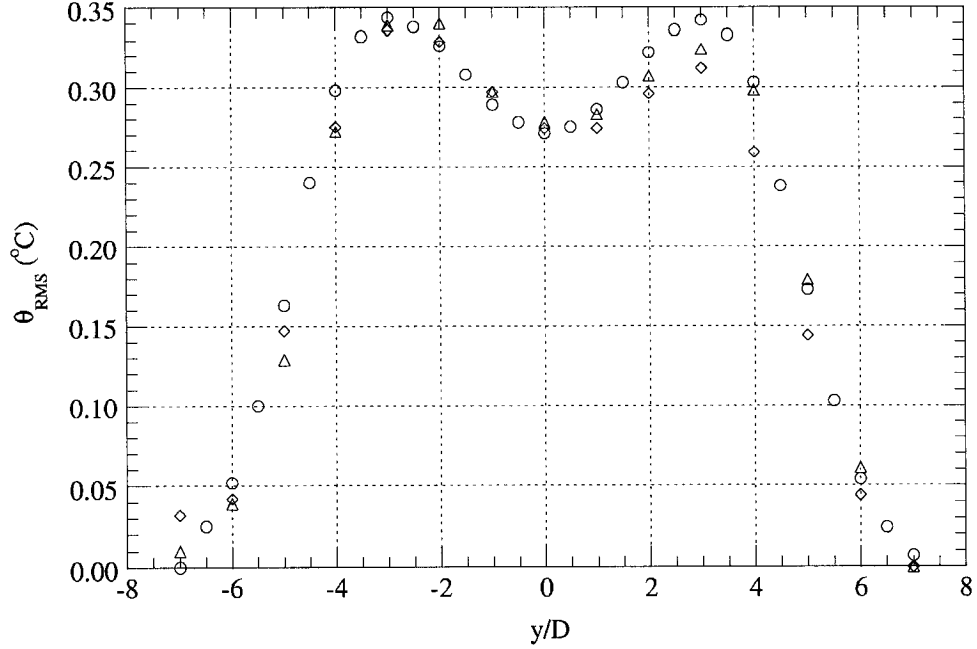


Figure 3.10: RMS profile of T for different heights. ($x/D = 53$). \circ : $z/D = 0$, \triangle : $z/D = -2$, \diamond : $z/D = -3.5$.

The temperature statistics (θ_{RMS} , S_θ , and F_θ) are constant within 2.5% along the cylinder axis for a portion of 4 diameters located at the mid-height. Figure 3.10 indicates that the RMS profile of temperature does not change significantly with height, the largest differences being around the peaks for $y > 0$.

The power spectral densities shown in Figure 3.11 indicates that the structure of the temperature is almost the same for different heights along the centreline. The largest difference is at small frequencies (large scales). These results suggest that, like the velocity field, the temperature is indeed independent of the z direction for a central portion of at least 7 diameters.

The same test could be made for the mandoline. However, the mandoline wires have a much larger length to diameter ratio ($l_{wire}/d_{wire} \simeq 6000$) and therefore end effects should be smaller and the temperature should be injected more uniformly in the z -direction.

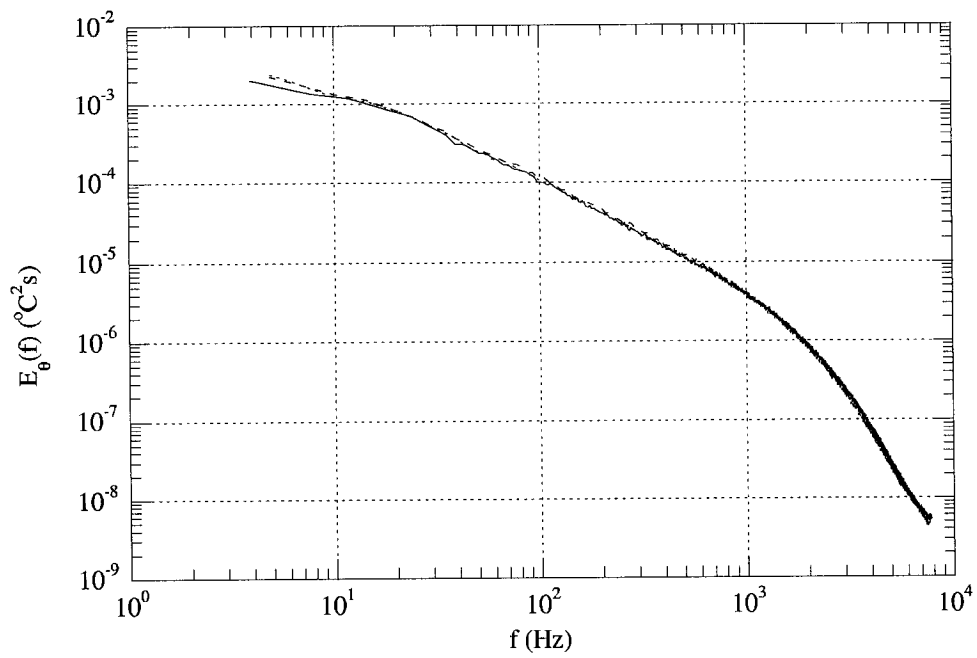


Figure 3.11: Power spectral density of T for different heights. ($x/D = 53$ and $y/D = 0$).

Chapter 4

The Effect of the Velocity Integral Scale on the Scalar Field

Studies in grid-generated turbulence have shown that the decay rate of the scalar fluctuations depends primarily on the ratio of the velocity field integral length scale at the injection point to the scalar injection scale (herein referred as ℓ_o/L_θ or the injection ratio). At this point, it is important to differentiate between the scalar injection scale, L_θ , and the velocity field integral length scale, ℓ_o . The latter is the actual integral scale of the velocity field at the injection point and can be computed as described in section 3.1. The scalar field is created at the injection point, x_θ , and its integral length scale cannot yet be computed. Therefore, the scalar injection scale refers to the physical configuration of the mandoline, i.e., its width and wire spacing. The idea of the scalar injection scale originates from Durbin[47]. Durbin estimated L_θ (ℓ_T in his text) by assuming $L_\theta = 0.2M_T$ (M_T is the wire spacing of the mandoline) in order to compare his theoretical results with the experiments of Warhaft and Lumley[24] (herein referred to as W&L) and those of Sreenivasan, Tavoularis, Henry, and Corsin[46] (herein referred to as STHC). The scalar injection scale is different from the integral length scale of the scalar field, ℓ_θ .

W&L showed that it is possible to vary the injection ratio by use of a mandoline. They varied the velocity integral scale by moving the mandoline downstream of the source of the turbulence (a grid) and also varied the scalar injection scale by changing the mandoline wire spacing. This chapter will extend W&L's work to an inhomogeneous free-shear flow by moving a mandoline of fixed size (fixed scalar injection scale) downstream in the wake of a cylinder. The effect will be a variation of the injection ratio by changing the velocity integral length scale. Emphasis will be put on the "response" of the scalar field to changes in the velocity field scale in the presence of the inhomogeneity. The results of changing the scalar injection scale will

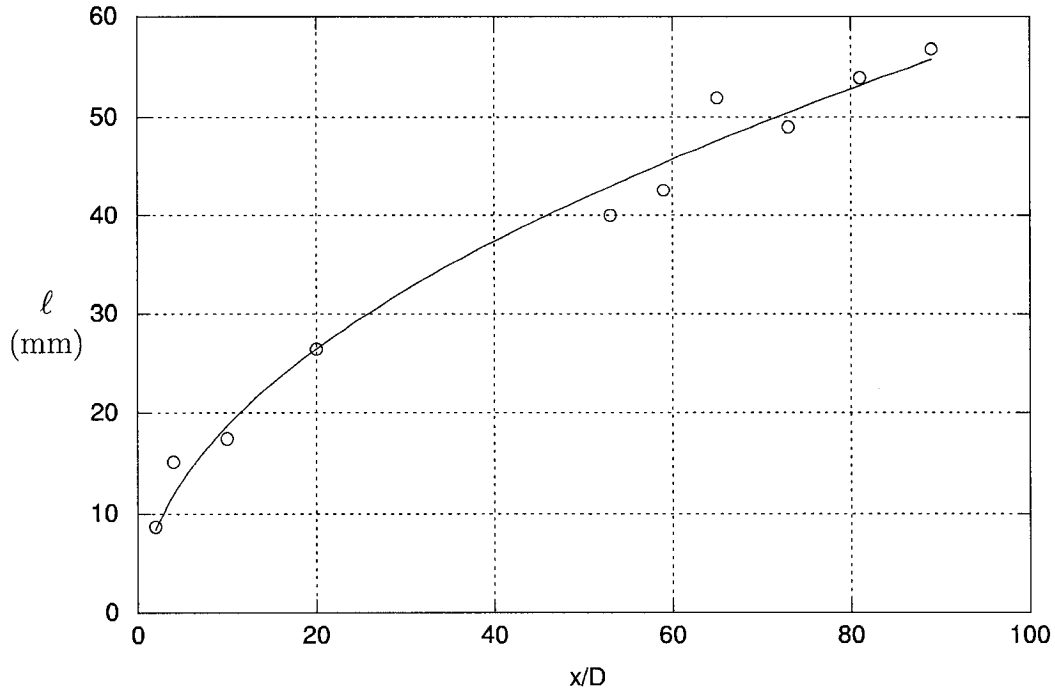


Figure 4.1: Evolution of the integral length scale of u downstream of the cylinder.

be presented in Chapter 5.

4.1 Evolution of the Velocity Integral Scale

To understand how the injection ratio influences the scalar field, it is important to study the downstream evolution of the velocity field length scales. The relevant velocity field scale is the integral length scale, ℓ . In the wake of a cylinder, ℓ is proportional to the half-width of the wake. ℓ increases in the downstream direction since the wake widens. Figure 4.1 displays the evolution of ℓ for different downstream positions (see §3.1 for details on how ℓ is computed). According to Tennekes and Lumley[9], ℓ should grow with the square root of x . The solid line in Figure 4.1, which represents a least-square fit of the form $\ell = b\sqrt{x/D}$, fits the data well over the entire range. Clearly, moving the mandoline downstream of the cylinder increases the injection ratio.

In this chapter, only the downstream position of the mandoline, x_θ , will be changed, which consequently changes the velocity scale at the injection point, ℓ_θ . The mandoline width is fixed to the diameter of the cylinder ($w/D = 1$). The wire spacing is fixed to $\frac{1}{10}$ of the cylinder diameter in order to have a good signal to noise ratio while keeping the flow blockage to an acceptable level. The choice for the width

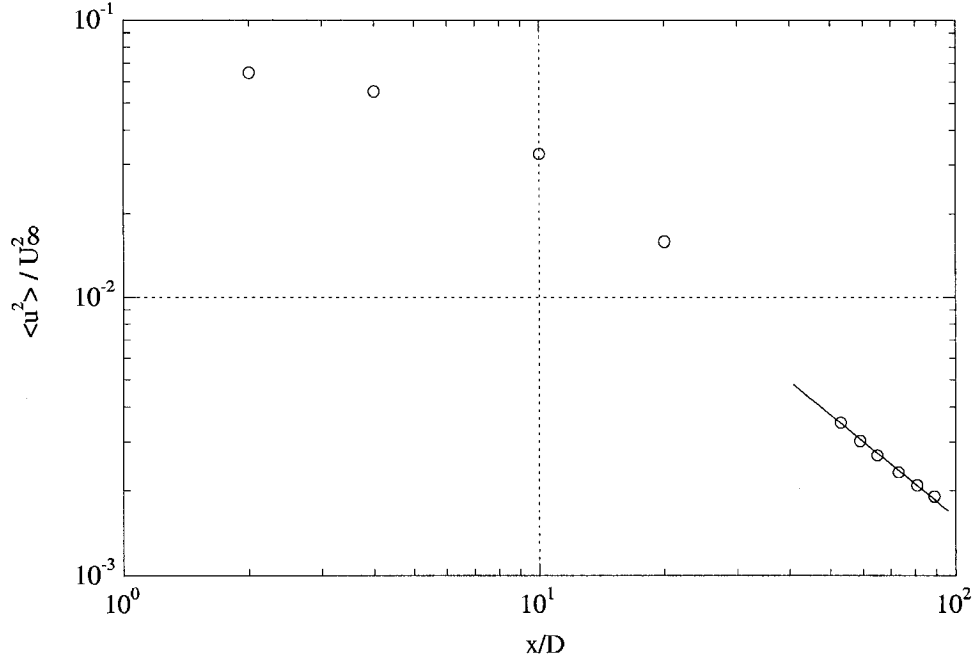


Figure 4.2: Decay of the variance of u downstream of the cylinder for the entire range of x/D .

of the mandoline appears to be natural. Léveque *et al.*[56] also used this width for their mandoline.

4.2 Decay Rate of the Scalar Variance

To gain a better understanding of the effect of the injection ratio on the scalar field, we first look at its downstream evolution. Using his dispersion theory[47], Durbin was able to show that, although the decay of fluctuating quantities is not described by a power-law for all downstream positions, there does exist a large range in which one holds. In Figure 4.2, the decay of the variance of u is shown over the entire range of downstream positions for this experiment. This range includes the early part of the decay of the velocity variance. It can be observed that a power-law regime exist for $x/D \geq 50$.

The range of downstream positions of interest is that where Figure 4.2 exhibits a power-law decay. Therefore, the next figures showing decay laws will be shown only for $53 \leq x/D \leq 89$. This is the case in Figure 4.3, where the decay of u^2, v^2 , and q^2 (the turbulent kinetic energy per unit mass), are plotted. The solid lines represent a power-law least-square fit of the form:

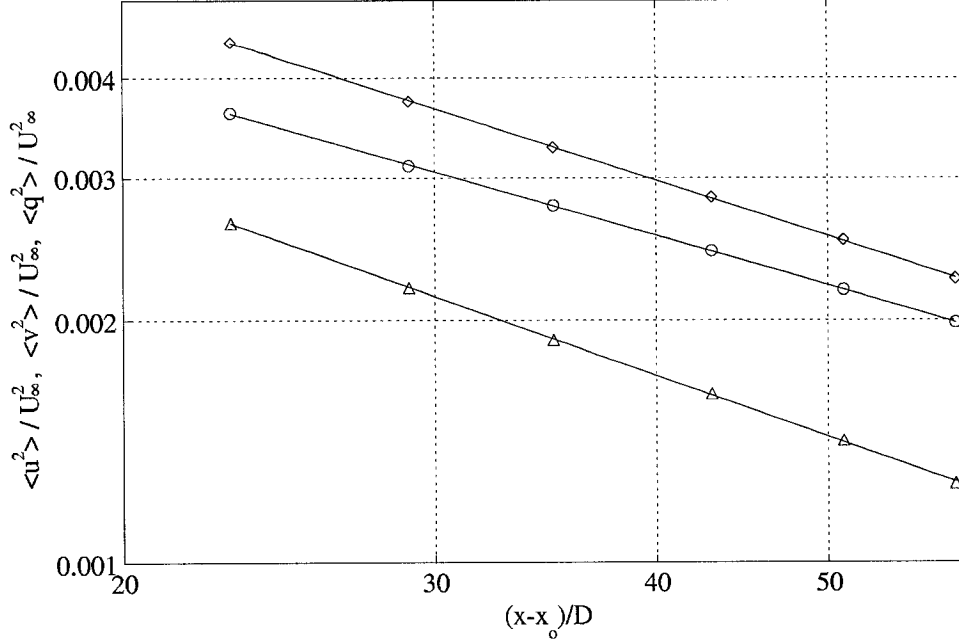


Figure 4.3: Decay of the velocity variance for the range under consideration herein. \circ : u^2 , \triangle : v^2 , \diamond : q^2 .

$$\frac{\langle u^2 \rangle}{U_\infty^2} = A \left(\frac{x - x_o}{D} \right)^{-n}. \quad (4.1)$$

This form has been often used in grid-generated turbulence, where the value of n is about 1.3. In this case, $n = 0.63$: half the value obtained in grid turbulence. The explanation is most likely that, in the case of the wake, turbulent kinetic energy is produced by the mean flow and therefore reduces the decay rate of the fluctuating kinetic energy. Also shown in Figure 4.3 is the decay rate of $\langle v^2 \rangle$, which is faster than that of u ($n = 0.78$ for v). The decay rate of the mean kinetic energy of the fluctuations, $\langle q^2 \rangle$ ($= \frac{1}{2}(\langle u^2 \rangle + \langle v^2 \rangle + \langle w^2 \rangle)$), is also well fitted by a power law (w is obtained by rotating the X-wire probe 90° about the x-axis). Since w decays at the same rate as v , the decay exponent for $\langle q^2 \rangle$ is 0.72, a value between that of u and v . The value for the virtual origin ($x_o/D = 30$) is larger than in grid turbulence (typically, $x_o/M \simeq 3$, where M is the mesh size of the grid - see for example W&L). This larger value for x_o/D might result from the developing region of the wake or of the von Kármán vortex street.

The same procedure is applied to the scalar field using a similar equation with different constants:

$$\frac{\langle \theta^2 \rangle}{\Delta T^2} = B \left(\frac{x - x_o}{D} \right)^{-m} \quad (4.2)$$

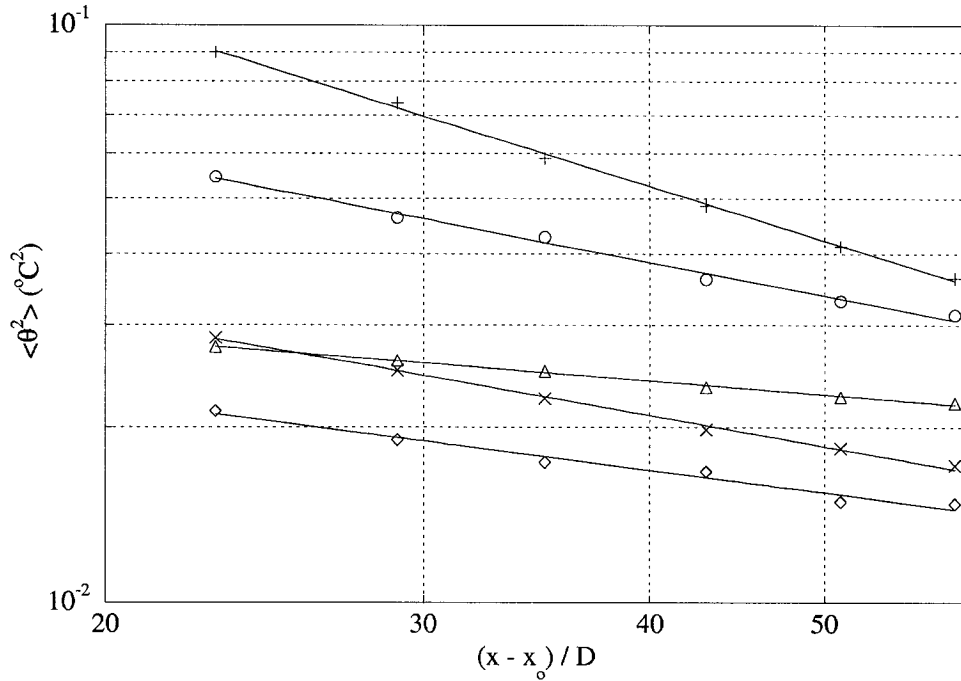


Figure 4.4: Decay of the temperature variance as a function of mandoline downstream position. \circ : Cylinder, \triangle : $x_{\theta}/D = 2$, \diamond : $x_{\theta}/D = 4$, \times : $x_{\theta}/D = 10$, $+$: $x_{\theta}/D = 20$.

where ΔT is the mean temperature excess ($\langle T \rangle - T_{\infty}$). W&L varied the downstream position of their mandoline and obtained different values for m which signifies a non-unique ratio of m/n . STHC also varied the downstream position of their heated screen (for a different range of downstream positions) and found that m was hardly affected, i.e., m was independent of ℓ_o and m/n was therefore unique. Durbin's dispersion theory shows that the relevant parameter governing m is the injection ratio, ℓ_o/L_{θ} [47]. According to Durbin, if $\ell_o/L_{\theta} \geq 2.5$, then m will be independent of ℓ_o .

The goal of this experiment is to study the effect of the velocity integral scale on the decay rate of the scalar, m , and other important parameters such as the ratio of mechanical to thermal time scales, r . Hence, ℓ_o needs to be kept small, i.e., the mandoline must not be positioned too far from the cylinder. Therefore, the range of mandoline downstream positions (x_{θ}) is chosen to be between 2 and 20 diameters. Figure 4.4 displays the decay of the scalar variance for the different mandoline positions and the decay of the scalar variance behind a heated cylinder for comparison.

The decay of the scalar variance is well fitted by the power-law described in Equation 4.2. In Figure 4.4, the scalar variance is not normalized by ΔT^2 because

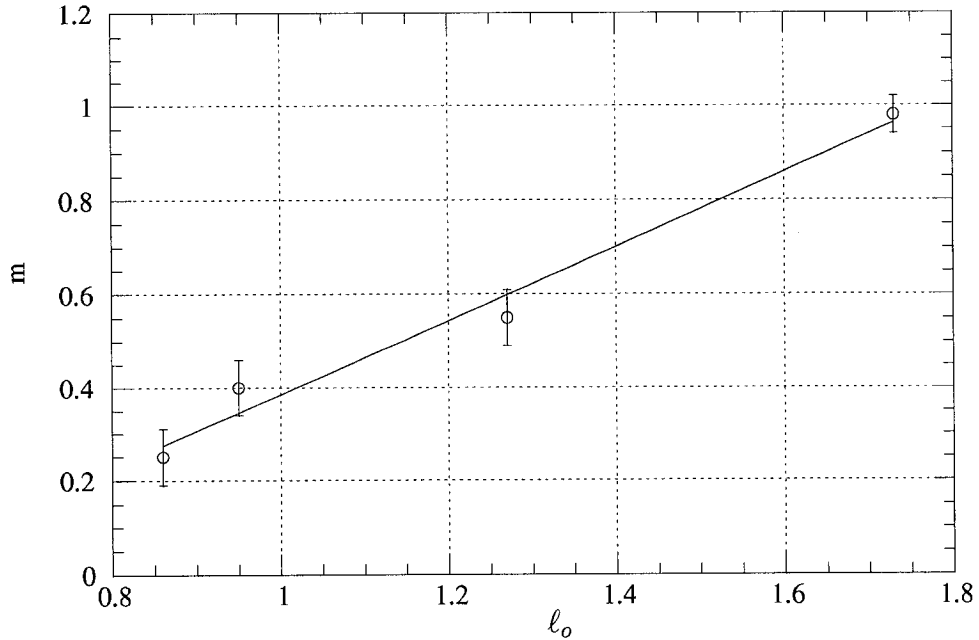


Figure 4.5: Decay rate exponent as a function of mandoline downstream position.

the latter could not be measured accurately. In a wake, ΔT^2 is a function of x/D . (Although the heat flux is conserved, the width of the wake increases.) However, the decrease in ΔT^2 is independent of x_θ . Therefore, computing m based on $\langle \theta^2 \rangle$ alone will not affect the following discussion.

The virtual origin, x_o , is the same as for the velocity and is independent of x_θ . The slope of the least-square power-law curve fits, m , in Figure 4.4 varies with mandoline position. An extensive study of the effect of the heat input revealed that m is independent of the initial fluctuation intensity. In addition, all the dimensionless statistics (S_θ , F_θ , PDF) and the structure of the flow are independent of the heat input. This independence is also the case for the cylinder.

Therefore, because m is not a function of the heat input but only a function of ℓ_o , it is meaningful to look at the relationship between m and ℓ_o . Figure 4.5 suggests no particular form, although a linear relationship (shown as the solid line) agrees well with the data.

4.3 Structure of the Scalar Field

Because the heat injection occurs at the large scales of the flow, the integral length scale of the scalar will be studied. The longitudinal integral length scale of the scalar field, $\ell_{\theta,x}$, is obtained exactly the same way as with u . In this chapter, the subscript

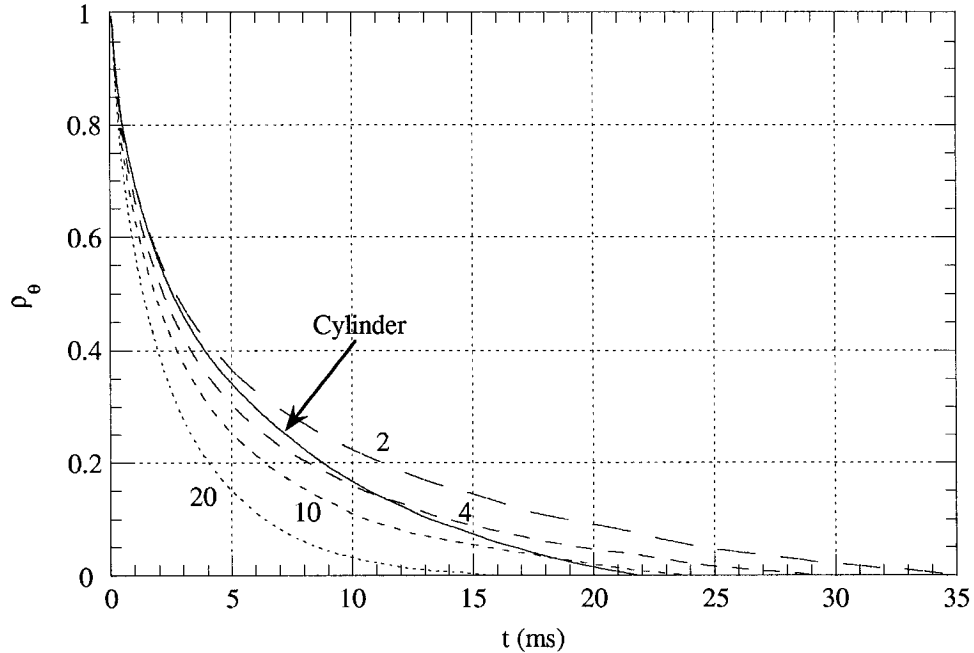


Figure 4.6: Auto-correlation of the temperature signal. ($x/D = 53$).

x is omitted since only the longitudinal scale is studied. The auto-correlation of θ , which is shown in Figure 4.6, clearly exhibits changes in ℓ_θ for different mandoline configuration. The results for ℓ_θ are shown in Table 4.1.

x_θ/D	ℓ_θ at $x/D = 53$	ℓ_θ at $x/D = 89$
2	54.4	78.1
4	45.1	60.8
10	34.9	54.3
20	22.6	37.7
Cylinder	47.2	63.5

Table 4.1: Effect of the mandoline's downstream position on ℓ_θ (dimensions are in mm).

The resulting scalar field has a smaller integral scale for increasing x_θ , which reinforces the idea that ℓ_o/L_θ is increased as x_θ is increased. Another way to consider the structure of the scalar field is to examine its power spectral density (or spectrum) since it displays the relative intensity of all the scales present in the field. The spectrum of the scalar field is shown in Figure 4.7 for the different x_θ . It is normalized by Kolmogorov (small-scale) variables in order to put emphasis on the relative differences at the large scales. The small scale collapse (high wavenumbers) is quite good except at the highest wavenumbers where electronic noise becomes significant. Differences appear at the large scales. The smallest (normalized) intensity occurs for the largest mandoline downstream position and it increases with decreasing x_θ .

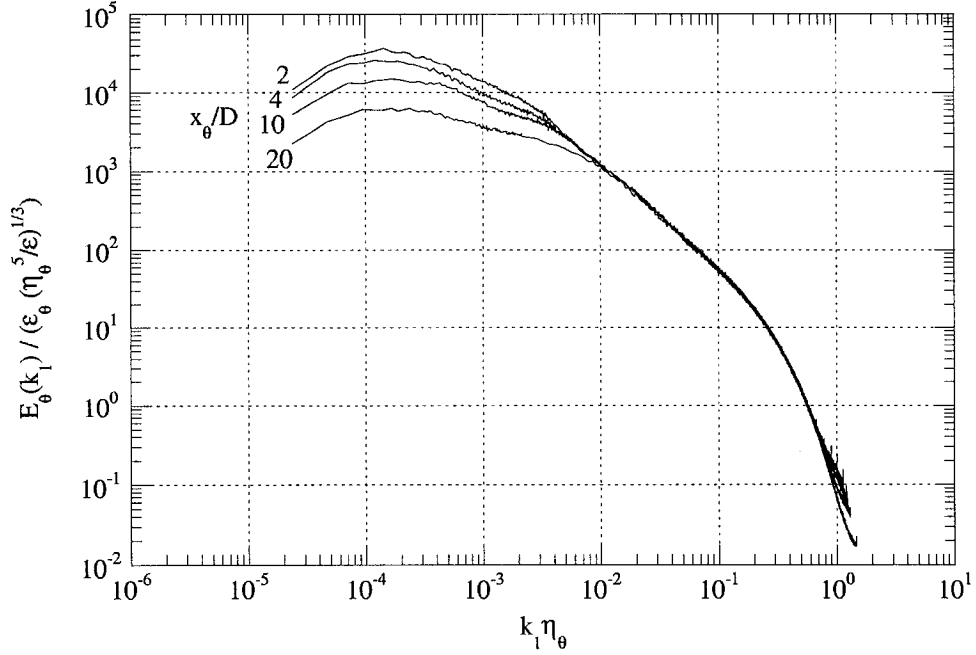


Figure 4.7: Spectra of the temperature field for different mandoline downstream positions. ($x/D = 53$).

The problem with one-dimensional spectra is that they suffer from large-scale aliasing, as discussed in Tennekes and Lumley[9] (see page 249). This aliasing renders more difficult the estimation of ℓ_θ from the spectrum. A solution is to study the three-dimensional spectrum. W&L assumed isotropy to derive the three-dimensional scalar spectrum from the longitudinal spectrum (see Tennekes and Lumley[9], page 281, Eq. 8.6.9) and used the three-dimensional spectrum to illustrate the changes in the integral length scale. The changes are represented by a shift in the peak of the three-dimensional spectrum (see their Figure 15).

Isotropic relations cannot be used in this anisotropic flow to obtain the three-dimensional spectrum from the longitudinal spectrum alone. However, it is suggested by Lumley and Panofsky[57] (see page 31) that, assuming an exponential decay for the longitudinal auto-correlation (which is inaccurate at the smallest separations), the wavenumber corresponding to the peak of $k_1 \times E_\theta$, k_{max} , is equal to the inverse of the integral length scale.

The curves in Figure 4.8 represent a smooth curve fit through the data points of Figure 4.7 (multiplied by the corresponding $k_1 \eta_\theta$). In Figure 4.8, the peak of $k_1 \times E_\theta$ is a function of $k_1 \eta_\theta$. As x_θ increases, the location of the peak is shifted toward larger $k_1 \eta_\theta$. This suggests that ℓ_θ decreases as x_θ increases.

k_{max} is determined by finding the zero of the derivative of $k_1 \times E_\theta$. The results for

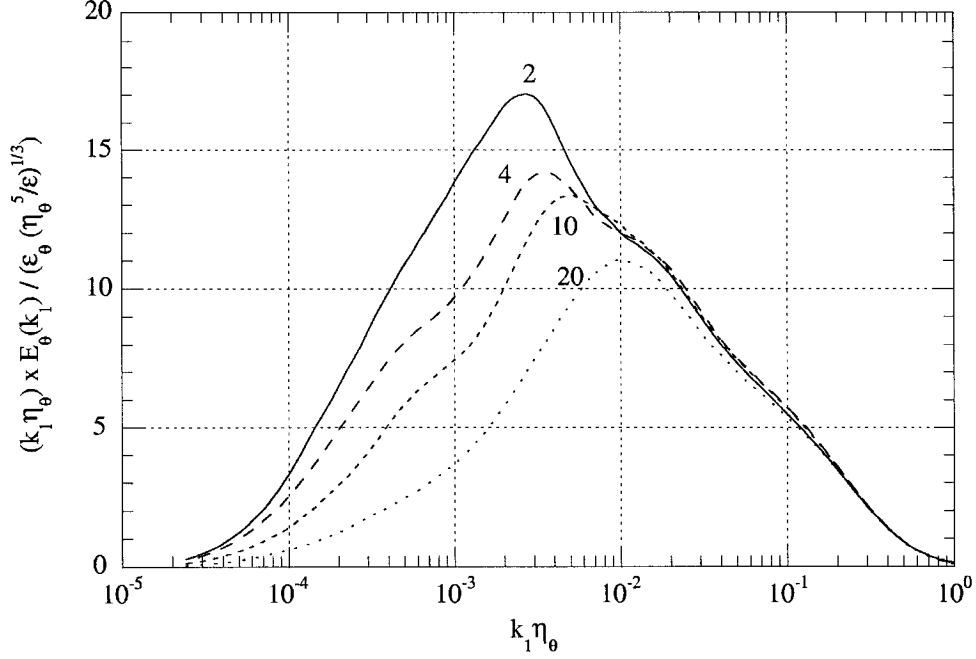


Figure 4.8: Spectra multiplied by the wavenumber for different mandoline downstream positions. ($x/D = 53$).

k_{max} versus m are shown in Figure 4.9 and appear to follow a logarithmic relationship, whereas W&L observed a linear relationship. However, in both cases, the relationship is far from certain due to the lack of data. In general, the behavior of both k_{max} and ℓ_θ support the fact that ℓ_o/L_θ increases as x_θ increases.

4.4 Time Scale Ratio

As noted by W&L, turbulent flows should have time and length scale ratios that are connected to each other by the mean flow, i.e., faster time scales should be related to smaller length scales. Therefore, the ratio (r) of the mechanical to thermal time scales (τ and τ_θ) will be studied and compared with the ratio of integral length scales (ℓ/ℓ_θ). r is defined as:

$$r = \frac{\tau}{\tau_\theta} = \frac{\langle q^2 \rangle / \epsilon}{\langle \theta^2 \rangle / \epsilon_\theta}. \quad (4.3)$$

In grid generated turbulence, since the velocity and thermal fields are homogeneous and isotropic, the variance budgets of the velocity and the scalar reduce to:

$$\frac{1}{2} \frac{d\langle q^2 \rangle}{dt} = -\epsilon \quad (4.4)$$

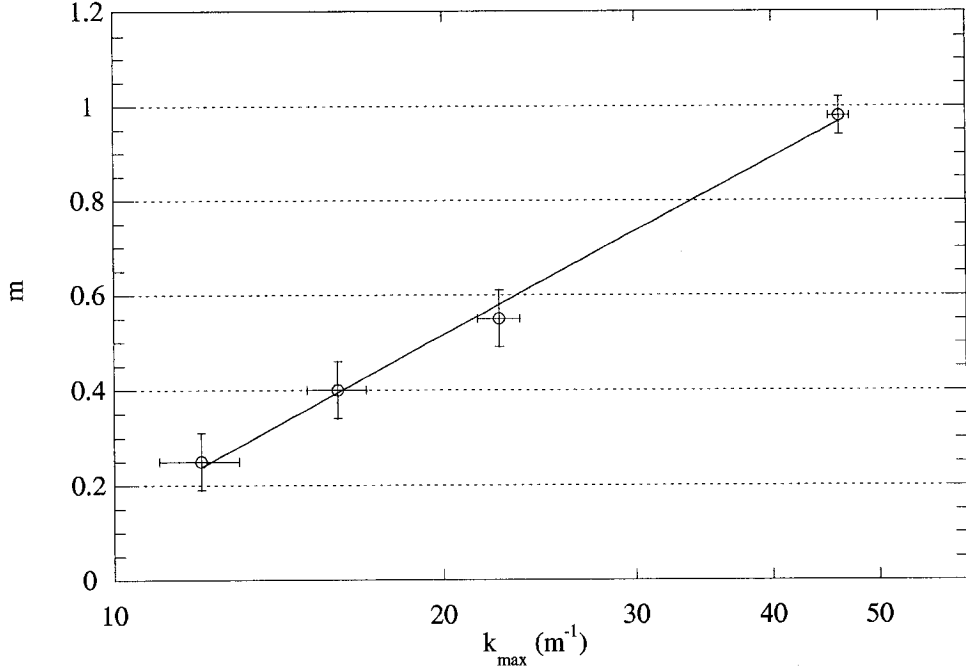


Figure 4.9: The decay exponent as a function of the wavenumber at the peak of $k_1 \times E_\theta$. ($x/D = 53$).

and

$$\frac{1}{2} \frac{d\langle\theta^2\rangle}{dt} = -\epsilon_\theta. \quad (4.5)$$

Hence, for this particular flow, it turns out that $r = m/n$. For the case of the wake, the turbulent transport term ($\frac{1}{2} \frac{\partial\langle v\theta^2\rangle}{\partial y}$) and the mean turbulent production term ($\langle v\theta\rangle \frac{\partial T}{\partial y}$) in the scalar variance budget are non-zero and cannot be neglected:

$$\frac{1}{2} \frac{d\langle\theta^2\rangle}{dt} + \frac{1}{2} \frac{\partial\langle v\theta^2\rangle}{\partial y} + \langle v\theta\rangle \frac{\partial T}{\partial y} = -\epsilon_\theta. \quad (4.6)$$

Therefore, such a simplification cannot be made ($r \neq m/n$). Equation 4.3 is used to evaluate r . The first thing to note is that r depends on the dissipation rate of turbulent kinetic energy (ϵ) and on the dissipation rate of the scalar variance (ϵ_θ). Figure 4.10 shows that the downstream evolution of ϵ_θ is also well fitted by a power-law (as is ϵ). m_ϵ (the decay exponent of ϵ_θ) follows the same trend as m with x_θ . Since all these experiments were conducted at the same free stream velocity, n_ϵ (the decay exponent for ϵ) is constant. Its value is 1.20 so that $n_\epsilon - n = 0.48$, which is considerably smaller than the theoretical prediction of 1 for homogeneous and isotropic turbulence.

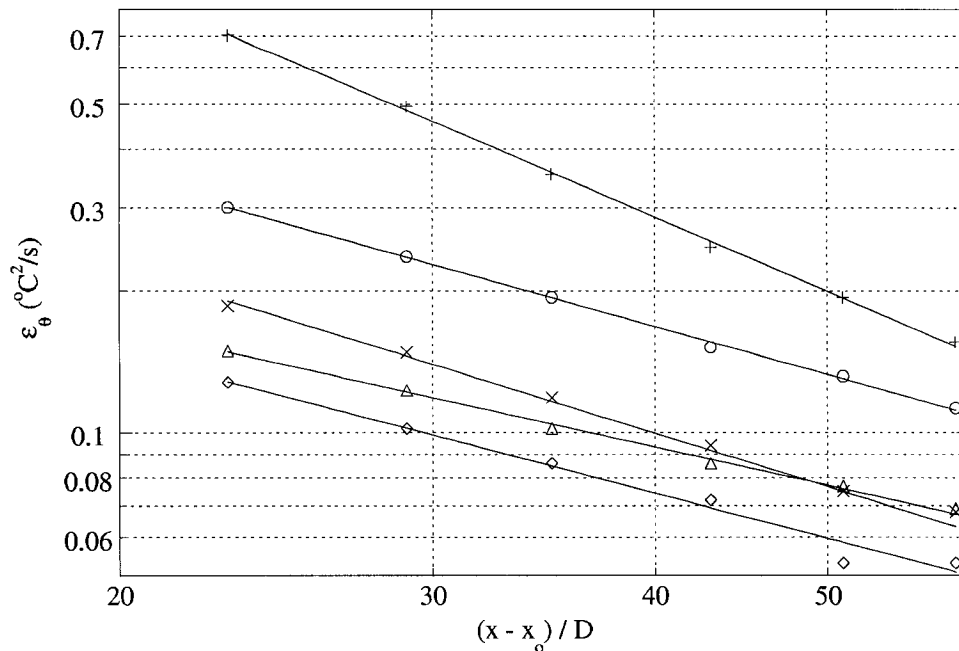


Figure 4.10: Decay of the scalar variance dissipation rate as a function of mandoline downstream position. ○: Cylinder, △: $x_\theta/D = 2$, ◇: $x_\theta/D = 4$, ×: $x_\theta/D = 10$, +: $x_\theta/D = 20$.

Since all the terms in the definition of r are well fitted by a power-law, r should also be described by a power law:

$$r = C (x/D - x_o/D)^{-n_r} . \quad (4.7)$$

In fact, the exponents of each variables in Equation 4.3 can be summed up to determine if r is constant downstream of the cylinder ($n_r = n - n_\epsilon - m + m_\epsilon$). Table 4.2 displays the decay rate of $\langle \theta^2 \rangle$ and of ϵ_θ along with n_r . n_r is very small for the cylinder and slightly larger than zero for all the mandoline cases. Although n_r is not zero, it is still half of the smallest value for m , which signifies that r should decrease very slowly downstream of the cylinder. The rate at which it decreases is similar for all mandoline positions.

To verify if all the previous observations are valid, the downstream evolution of r is plotted in Figure 4.11. It is not clear whether or not r decreases due to the experimental scatter, with the possible exception of $x_\theta/D = 20$. It should be noted that r is difficult to estimate accurately and that Sirivat and Warhaft[58] as well as Zhou *et al.*[21] measured r the same way and obtained experimental error of the same magnitude. Since r is ill-conditioned and because it decreases quite slowly, an average r is defined:

x_θ/D	m	m_ϵ	n_r
2	0.25	0.84	0.11
4	0.40	0.99	0.11
10	0.55	1.17	0.14
20	0.98	1.63	0.17
Cylinder	0.61	1.05	-0.04

Table 4.2: The decay exponents of the scalar variance and its dissipation rate. m_ϵ is the decay exponent of ϵ_θ . Note that $n = 0.72$ and $n_\epsilon = 1.20$.

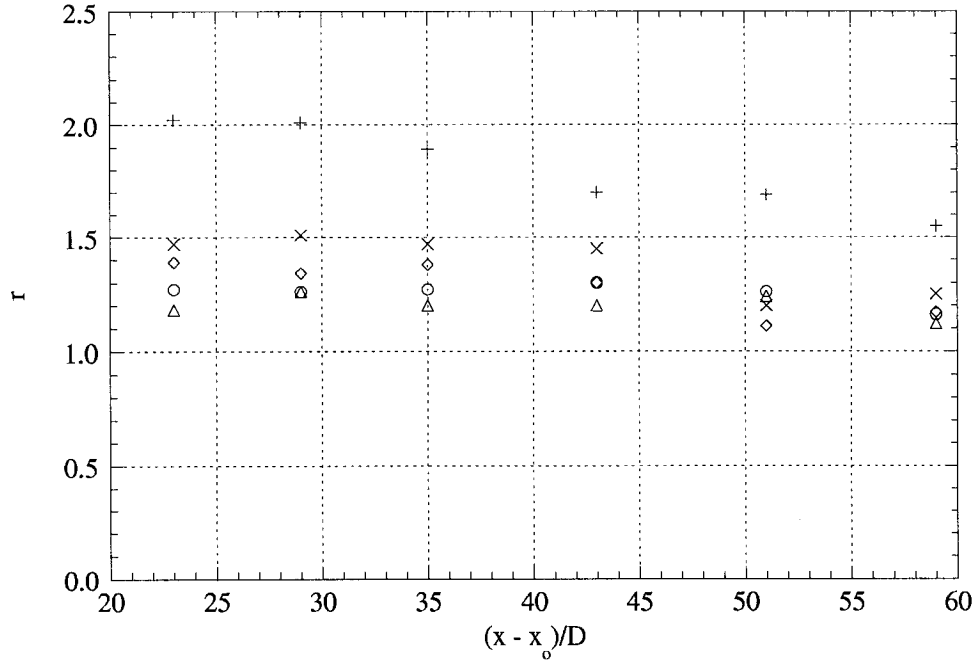


Figure 4.11: The time scale ratio r as a function of downstream position. \circ : Cylinder, Δ : $x_\theta/D = 2$, \diamond : $x_\theta/D = 4$, \times : $x_\theta/D = 10$, $+$: $x_\theta/D = 20$.

$$r_{avg} = \int_{53}^{89} r d(x/D). \quad (4.8)$$

This r_{avg} is used to compare the time scale ratio with the integral length scale ratio (ℓ/ℓ_θ , not the injection ratio). Figure 4.12 shows that r_{avg} increases when ℓ/ℓ_θ increases. As pointed out by W&L, smaller length scales should have faster time scales. Figure 4.12 is consistent with this idea.

W&L were able to collapse the peak of their three-dimensional spectra by normalizing the x-axis with r . Here, the peak of $k_1 \times E_\theta$ approximately collapses to the same wavenumber when the x-axis is normalized not by r_{avg} but by m (shown in Figure 4.13). The largest error comes from the case of $x_\theta/D = 2$ and is expected since the value of m obtained for this case is also low. It should be noted that, in

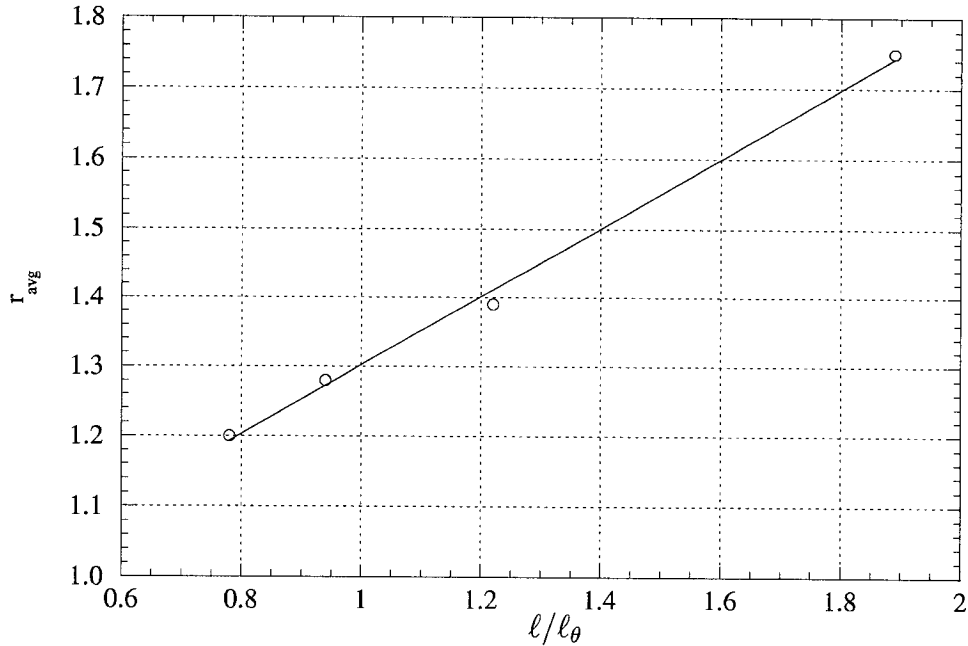


Figure 4.12: The time scale ratio r as a function of the ratio of the velocity to scalar integral length scales.

the case of W&L, $r = m/n$ so that the peak of their three-dimensional spectra would also collapse if the x-axis were normalized by m (given that n is also a constant in their flow).

4.5 Longitudinal Velocity-Scalar Correlation

As pointed out by W&L, the mandoline is a physical apparatus designed to decouple the temperature field from the velocity field. To examine the coupling between these two fields, we study the correlation coefficient of the longitudinal velocity fluctuation and the scalar fluctuation ($\rho_{u\theta}$). For the case of the cylinder, there exists a naturally high anti-correlation ($\rho_{u\theta} \simeq -0.35$) that results from the von Kármán vortex street, as explained by Matsumura and Antonia[36]. The hot fluid originates from the wake close to the cylinder and is therefore slower than the cold fluid coming from the free stream, thus producing the natural anti-correlation.

The relatively large anti-correlation between u and θ for the heated cylinder is expected because, as in the case of heated grids, the turbulence source and the heat source are the same. To verify whether the mandoline decouples the two fields, Figure 4.14 displays the downstream evolution of $\rho_{u\theta}$ for the cylinder and the same four mandoline positions. The maximum anti-correlation (largest $|\rho_{u\theta}|$) occurs for $x_\theta/D = 4$ where the von Kármán vortex street is strongest. This persistent anti-correlation is

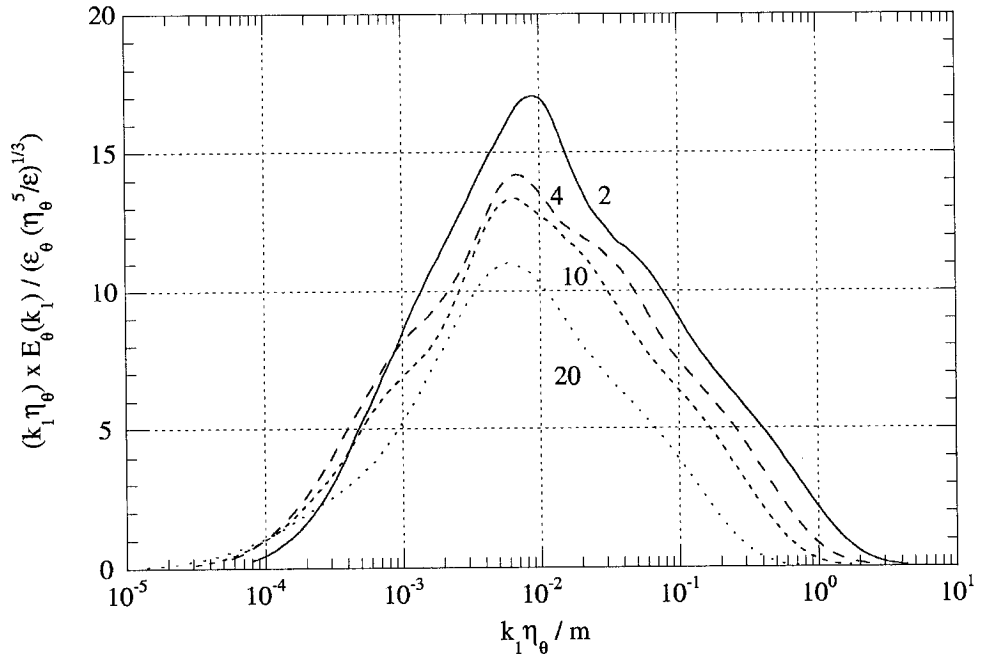


Figure 4.13: The spectrum multiplied by the wavenumber for different mandoline downstream positions.

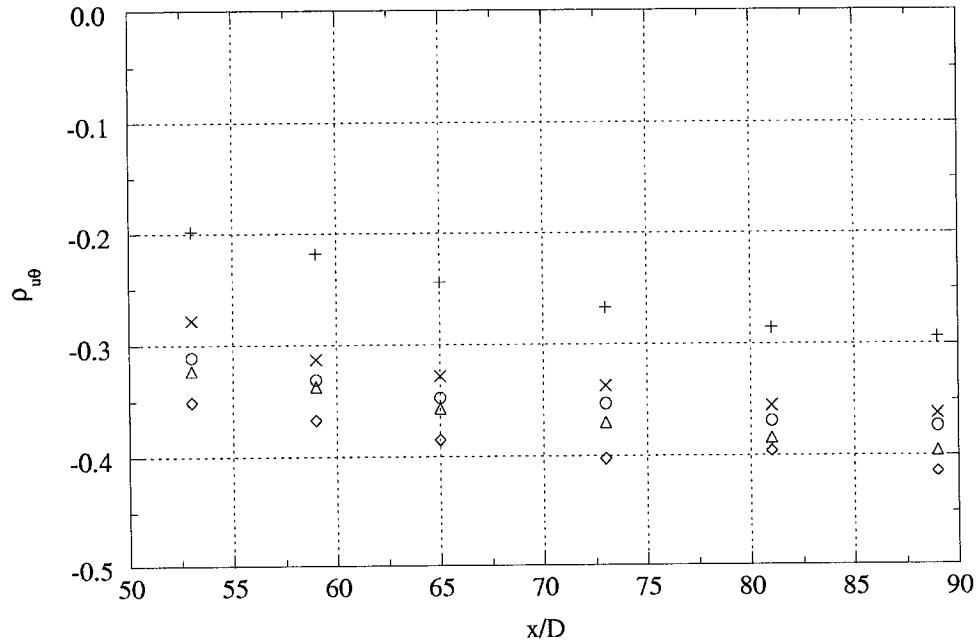


Figure 4.14: The cross-correlation coefficient as a function of downstream position. \circ : Cylinder, \triangle : $x_\theta/D = 2$, \diamond : $x_\theta/D = 4$, \times : $x_\theta/D = 10$, $+$: $x_\theta/D = 20$.

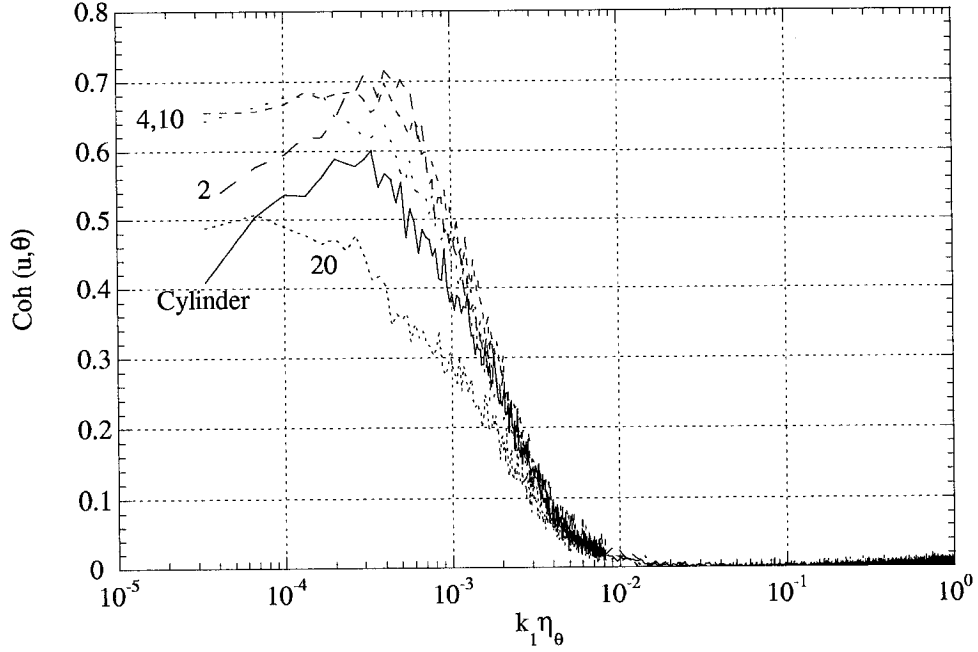


Figure 4.15: The coherence of the temperature field as a function of mandoline downstream position. ($x/D = 53$)

very different from W&L where the anti-correlation was significantly smaller for the mandoline than for the heated grid. To understand the mechanism behind this anti-correlation, it is useful to look at the coherence of the signal ($Coh(u, \theta) = |E_{u\theta}|^2 / (E_u \times E_\theta)$).

Like in W&L, Figure 4.15 indicates that the anti-correlation originates from the large-scale structure. The coherence for the mandoline cases is of the same order of magnitude as for the heated cylinder. The reason for the anti-correlation persisting in the case of the mandoline is the structure of this flow. The mandoline heats the slow fluid behind the cylinder, i.e., it heats the vortices. As x is increased, the relatively slow fluid is hot, and the fast fluid, coming from the potential flow is cold, producing this anti-correlation. As x_θ is increased, $|\rho_{u\theta}|$ decreases. This attenuation in the anti-correlation might be because the mandoline heats some of the fast engulfed fluid or because the vortex is larger than the mandoline and it is therefore not heated completely. Both effects would reduce the strength of the anti-correlation. Thus, we observe that the structure of this inhomogeneous decaying flow is significantly different than that of homogeneous, isotropic grid turbulence.

Chapter 5

The Effect of the Scalar Injection Scale on its Field

As seen in Chapter 4, the decay rate of the scalar fluctuations and the structure of its field are dependent on the injection and time scale ratios. In this chapter, the scalar injection scale (L_θ) will be independently varied. In grid-generated turbulence, W&L varied the scalar injection scale by varying the spacing between the wires of the mandoline. Doing so, they observed changes in the scalar field and its decay rate. STHC also varied the spacing between the wires of their heated screen, but the effect on the decay rate of the scalar variance was marginal because their wire spacings were too small compared to ℓ_o . That was not the case for W&L, where the different wire spacings were larger than the integral length scale of the velocity field.

In the wake of a cylinder, ℓ is of the order of the wake half-width so that the width of the mandoline is of the same order. Thus, it is impossible to produce changes in the wire spacing of the mandoline that would be larger than ℓ_o . Nevertheless, an extensive study about the effects of the wire spacing on the structure of the scalar field and the decay rate of its variance was carried out. As expected, it revealed that, for all mandoline downstream positions, doubling and even quadrupling the wire spacing only causes marginal effects on the scalar field and its downstream evolution.

Another way to vary the scalar injection scale was sought out. The wake is a free shear flow: it has no solid boundary. In other words, the domain of the turbulence is not clearly defined like, for example, in channel flow. Hence, it is impossible to heat all, but only, the turbulent flow. One has to make the choice of heating all the turbulent flow and heating some of the free stream or heat no free stream but letting some of the turbulent flow remain unheated. Because of these considerations, the choice of the width of the mandoline is non-trivial. In chapter 4, the width of

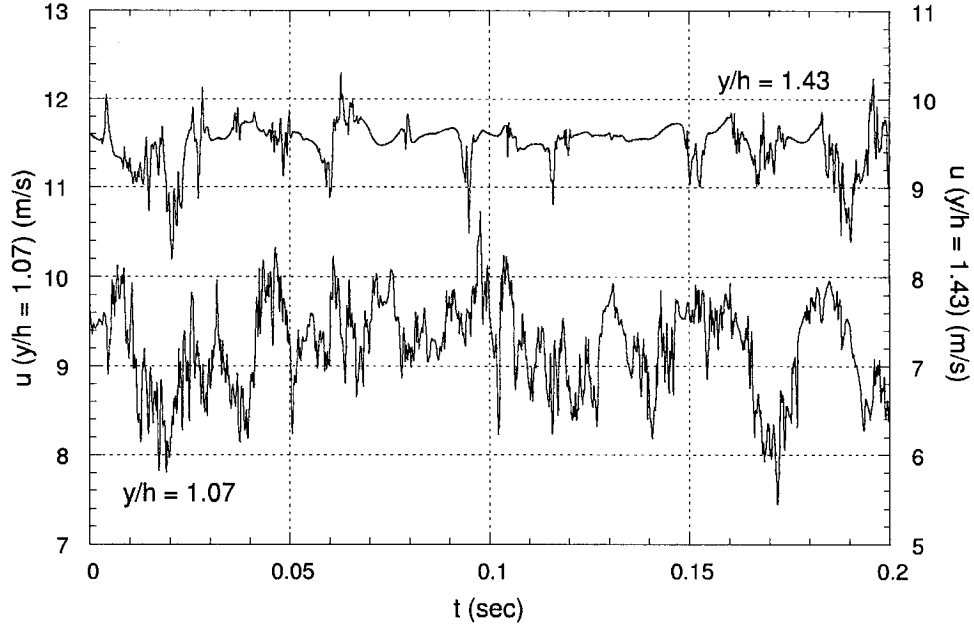


Figure 5.1: Typical time histories of u . $x/D = 53$ and $h/D = 2.7$

the mandoline is set equal to the cylinder diameter because i) such a choice seemed sensible, and ii) this width is what other researchers have chosen[56]. This chapter will study the effect of the width of the mandoline on the scalar field for a constant wire spacing ($s/D = 0.2$) and a constant mandoline downstream position ($x_\theta/D = 20$). Other downstream positions and wire spacings were studied, but the results were no different from the case treated here.

Three mandoline widths are selected: $w/D = 1, 2,$ and 3 . Since these changes in width are larger than ℓ at this downstream position ($\ell/D = 1.04$ at $x/D = 20$), noticeable effects are expected on the scalar field.

It seems important to specify whether the mandoline is heating the free stream for the largest w . The half-width of the wake (h , is defined as the lateral distance from the centreline to the point where the mean flow velocity defect is half that of the centreline), is growing at a rate slightly faster than the square root of x . It is equal to 1.72 diameters at $x/D = 20$ (somewhat larger than ℓ) so that the two half-widths occupy 3.44 diameters, larger than the maximum width of the mandoline. Figure 5.1 displays two typical time histories of the longitudinal component of velocity, u , at $y/h = 1.07$ and 1.43 for $x/D = 53$. At $y/h = 1.07$, there is no intermittency of the flow as there is for $y/h = 1.43$, which indicates that the flow remains continuously turbulent up to, at least, the half-width of the wake. It seems reasonable that if the flow remains fully-turbulent at the wake half-width at $x/D = 53$, it should be the

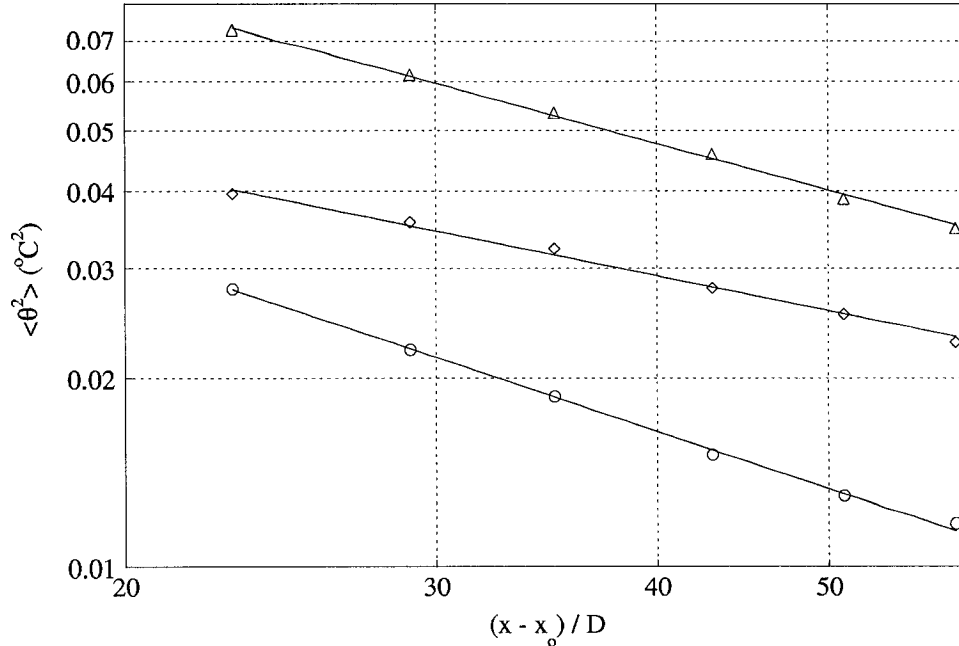


Figure 5.2: The effect of the w on the decay rate of $\langle \theta^2 \rangle$. \circ : $w/D = 1$, \triangle : $w/D = 2$, \diamond : $w/D = 3$.

same for $x/D = 20$. Therefore, even for the largest width, the mandoline never heats the potential flow.

5.1 Decay Rate of the Scalar Variance

To understand the effect of varying the width of the mandoline, we first consider the decay rate of the scalar variance. In Figure 5.2, the decay of $\langle \theta^2 \rangle$ is also well-fitted by a power law. As the width of the mandoline increases, the decay rate decreases. This behavior is consistent with the idea that increasing w is similar to increasing the scalar injection scale, L_θ . In W&L, the same effect was observed when the wire spacing was increased: increasing L_θ decreases the decay rate. This is the opposite to the velocity length scale, as expected, because the relevant parameter is not the length scale itself but the injection ratio, ℓ_o/L_θ , as discussed by Durbin[47].

Given that the decay exponent m is independent of the heating power of the mandoline, it is reasonable to consider the relationship between w and m . Figure 5.3 suggests that the variation of m with w is linear. Though there are only 3 data points in this figure, this result is supported by measurements at other x_θ . Therefore, the decay rate is proportional to the injection ratio.

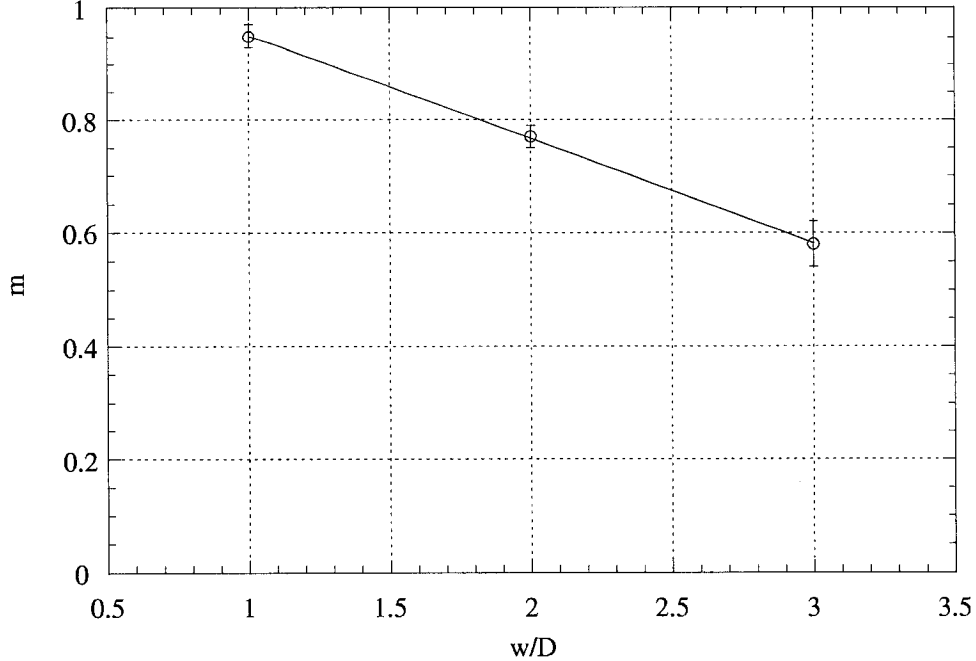


Figure 5.3: The decay rate as a function of the width of the mandoline.

5.2 Structure of the Scalar Field

It is now clear that changing the width of the mandoline has some effect on the downstream evolution of the scalar field. Typically, these changes are associated with changes in the structure of the scalar field. Therefore, $\ell_{\theta,x}$ will be examined here. It is computed using the auto-correlation of θ (see Figure 5.4). Changing the width produces very small changes in ρ_θ indicating that $\ell_{\theta,x}$ is not affected by the width of the mandoline. This independence of ℓ_θ is supported by the fact that k_{max} is not affected by w either (see Figure 5.5).

These results seem to contradict the observed changes in the decay rate. However, the wake is an inhomogeneous flow and there may be more than one integral length scale present in the flow. The fact that, changing the width of the mandoline produces physical changes in the transverse direction is a motivation to consider the transverse integral length scale, which is computed exactly the same way as the longitudinal one. As a starting point, the transverse integral length scale of the velocity field, $\ell_{u,y}$, will be examined. The transverse auto-correlation of u for two downstream locations is shown in Figure 5.6. The integration yields a length scale of 1.12 and 1.59 diameters at $x/D = 53$ and 89, respectively, while $\ell_{u,x}$ is 1.68 and 2.22 diameters for the same downstream positions.

The transverse auto-correlation is measured by keeping one probe at the centre-

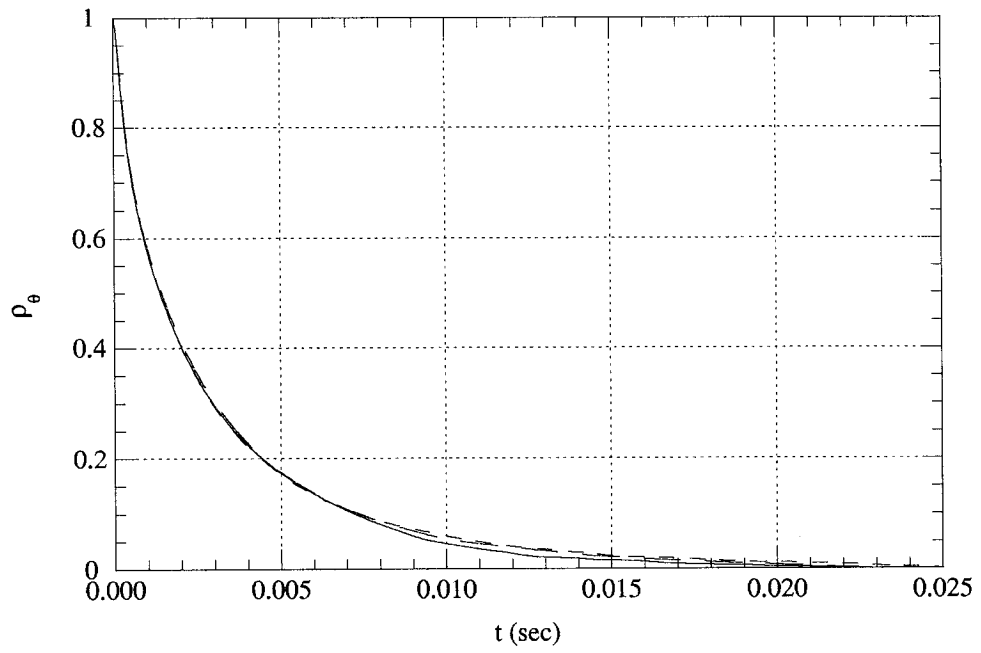


Figure 5.4: The auto-correlation of temperature for the three different mandoline widths.

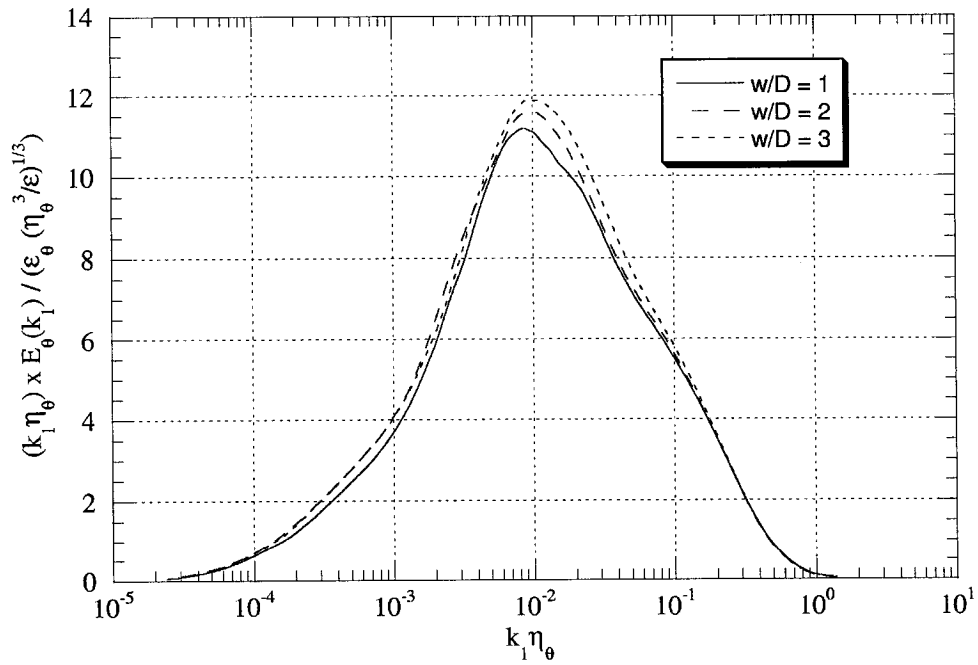


Figure 5.5: Spectrum multiplied by the wavenumber for different mandoline widths. ($x/D = 53$).

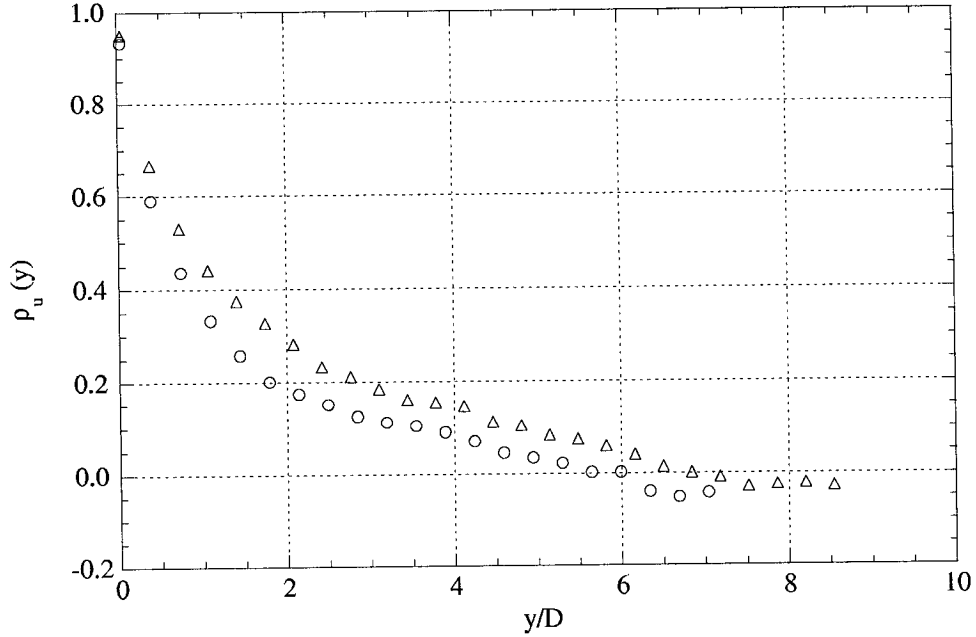


Figure 5.6: The transverse auto-correlation of u . \circ : $x/D = 53$, \triangle : $x/D = 89$.

line of the wake and moving a second one. To the author's knowledge, the transverse auto-correlation has never been measured in a wake. Because the wake is inhomogeneous in the y -direction, the auto-correlation is expected to be a function of y . Therefore, a new question arises: What is the proper methodology to measure the transverse auto-correlation? The method used here is to hold one probe at a fixed cross-stream location and to move the other one in the y -direction until it is completely outside of the wake. This method is used since only one traversing mechanism was available such that the two probes could not be moved simultaneously. To determine the effect of the fixed probe position on $\rho_\theta(y)$ (and consequently $\ell_{\theta,y}$), several tests are made measuring $\ell_{\theta,y}$ for the case of the heated cylinder, but this discussion is also valid for $\ell_{u,y}$ and any other mandoline configuration. The results from those tests are shown in Figure 5.7. In addition, an attempt at moving the two probes simultaneously but manually, is made in order to compare the results with the fixed probe method.

The effects of different measurement methods are not negligible. However, it is of interest to note that when employing the method where two probes are moving apart, the auto-correlation is always equal to the greatest value obtained when only one probe moves. The most reasonable method for measuring the auto-correlation at a point would be to move the two probes simultaneously, keeping the point at which the auto-correlation is wanted as the center of the probe separation. However, the

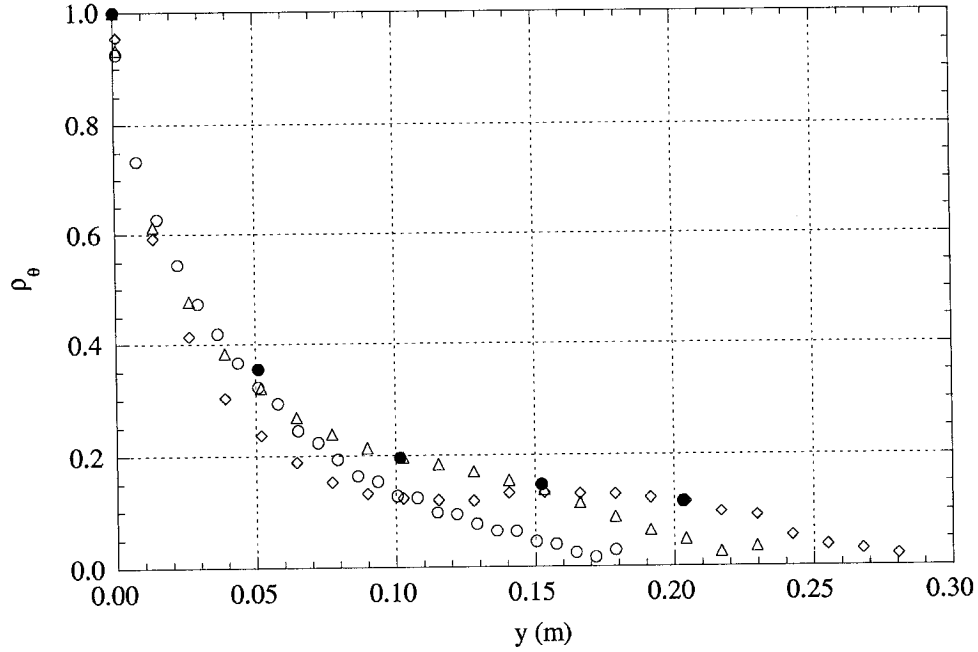


Figure 5.7: The transverse auto-correlation of T for the cylinder. $x/D = 53$. Fixed probe at: \circ : centreline, Δ : $y/D = -2$, \diamond : $y/D = -4$, \bullet : No fixed probe.

discussion here does not require exact estimates of the value of the length scale itself. In addition, the auto-correlation with no fixed probe can be deduced from the ones with fixed probe at different cross-stream locations. For the discussion here, only the auto-correlation of θ with the fixed probe at the centreline will be shown, but the other fixed probe positions were measured and did not provide any additional information of use.

For comparison purposes, the transverse auto-correlations of θ for the mandoline positions treated in Chapter 4 are shown in Figure 5.8. The same trend appear in this figure as it appeared for the longitudinal auto-correlation shown in Figure 4.6: the transverse integral length scale ($\ell_{\theta,y}$) decreases as x_θ increases. In fact, the transverse and longitudinal integral length scales are similar in this case. The results for $\ell_{\theta,y}$ are compared to the ones of $\ell_{\theta,x}$ for one downstream position in Table 5.1.

From the above discussion, it can be concluded that the measurements for $\ell_{\theta,y}$ give sensible results. Thus, $\ell_{\theta,y}$ can be used to study the effects of w on the structure of the scalar field. The results shown in Figure 5.9 for the transverse auto-correlation indicate that, like for the case of the longitudinal scale, there is little difference in $\ell_{\theta,y}$ caused by the change in w . These results suggest that the transverse length scales are not independent from the longitudinal ones.

Some conclusions can be made from the above results. Because ℓ_θ is independent

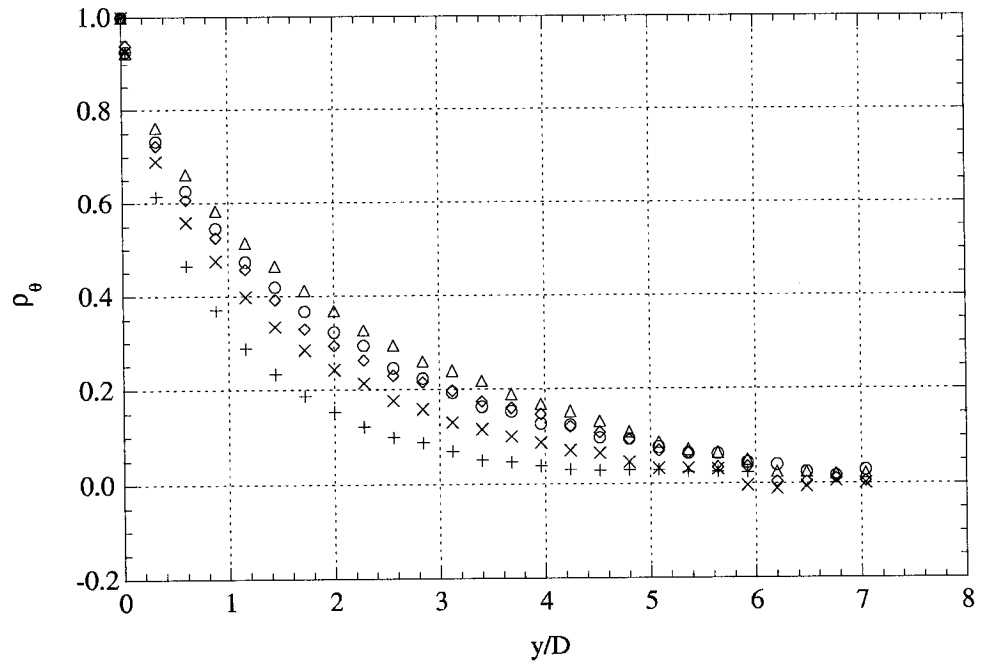


Figure 5.8: The transverse auto-correlation of T for different mandoline downstream positions. $x/D = 53$. \circ : Cylinder, Δ : $x_\theta/D = 2$, \diamond : $x_\theta/D = 4$, \times : $x_\theta/D = 10$, $+$: $x_\theta/D = 20$.

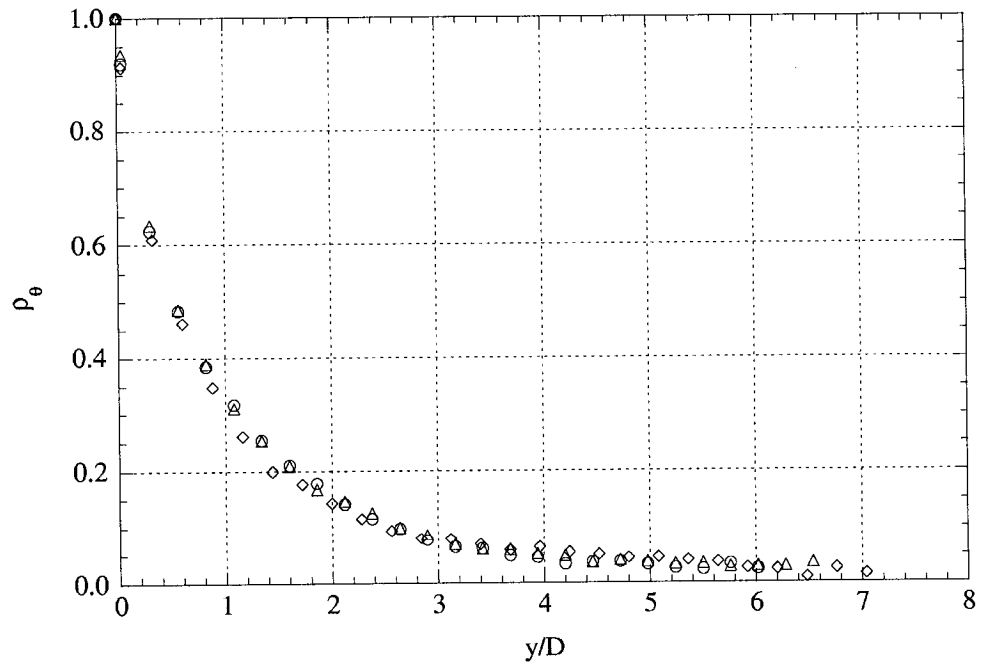


Figure 5.9: The transverse auto-correlation of T for different mandoline widths. $x/D = 53$. \circ : $w/D = 1$, Δ : $w/D = 2$, \diamond : $w/D = 3$.

x_θ/D	$\ell_{\theta,x}$	$\ell_{\theta,y}$
2	54.4	48.4
4	45.1	41.7
10	34.9	34.3
20	22.6	25.7
Cylinder	47.2	43.7

Table 5.1: Comparison between the longitudinal and the transverse integral length scale of the scalar field. ($x/D = 53$)

of the width of the mandoline (and the wire spacing), it is independent of the number of thermal sources in the wake, as long as they are all located at the same downstream position. Therefore, it would be reasonable to say that a mandoline of only one wire (a single line source) would produce the same ℓ_θ . This hypothesis could be possible since the equation governing the passive scalar field is linear so that the notion of superposition is applicable. ℓ_θ would not be affected by the superposition of the other plumes. However, this hypothesis was not verified and there may be some restrictions (e.g., only symmetric (about the centreline) mandolines were studied so that there could be some asymmetry effects on ℓ_θ).

5.3 Time Scale Ratio

Since changes in w produce sensible variations in m but only marginal differences in ℓ_θ , it is important to consider how the time scale ratio, r , reacts to changes in the width of the mandoline. It is not clear how r is affected by w . Here again, the decay of ϵ_θ is well fitted by a power-law such that n_r can be computed. For all three cases, it is at most 0.13 indicating again, a very slow decay of r . The slow downstream evolution of r is shown in Figure 5.10 again supporting the use of r_{avg} .

The values obtained for r_{avg} are 1.75, 1.83, and 1.68 for $w/D = 1, 2,$ and 3 , respectively. It is unclear whether these variations are significant because of the large experimental scatter in r . There is certainly no trend in r_{avg} with w like there is for m . This may seem to be contradictory because, until this work, studies involving the decay rate of the scalar variance were done in homogeneous, isotropic turbulence where the decay rate m and the time scale ratio r are directly linked due to the simplifications in the kinetic energy and scalar variance budgets. In the case of the wake, the turbulent transport and the mean scalar production terms play a capital role in decoupling r from m .

In addition, as pointed out in Chapter 4, r_{avg} should be proportional to ℓ/ℓ_θ

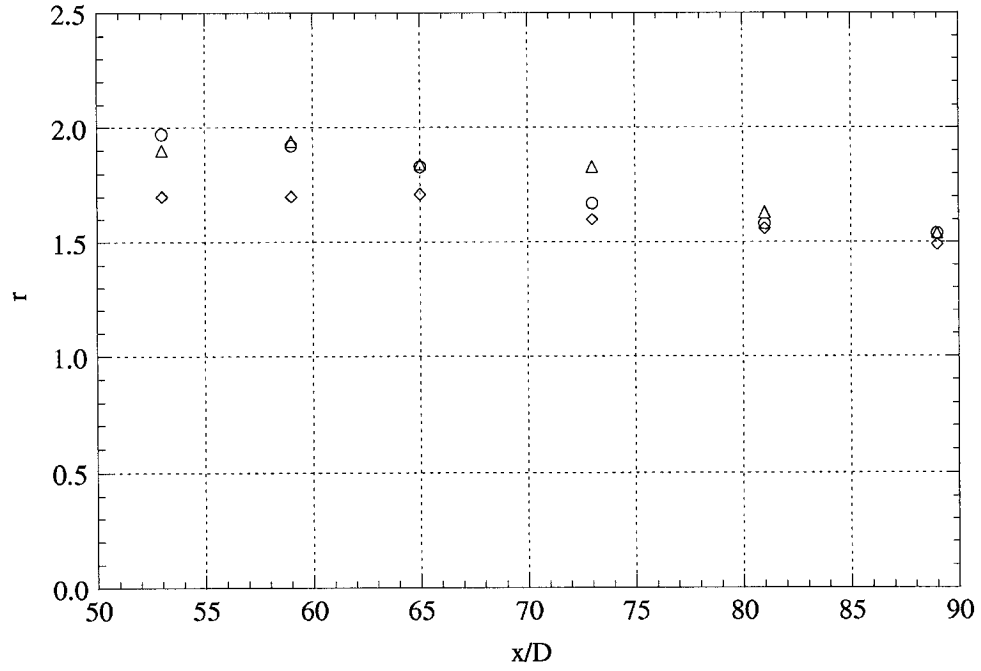


Figure 5.10: The downstream evolution of the time scale ratio for different mandoline widths. \circ : $w/D = 1$, \triangle : $w/D = 2$, \diamond : $w/D = 3$.

since faster time scales are associated with smaller length scales. Therefore, if ℓ_θ is found to be independent from w , r_{avg} should also be independent from it. Varying the width of the mandoline does not affect either, the time scale or the length scale of the scalar field at the centreline of the wake.

Chapter 6

Conclusions

The purpose of this work was to study the effects of the inhomogeneity of the flow and the injection ratio on the structure and the downstream evolution of the scalar field. This goal was accomplished first by varying the velocity integral length scale at the injection point only and then varying the scalar injection scale while keeping the velocity scale constant. To study the effects of the inhomogeneities, the injection ratio was varied in the wake of a cylinder and the results were compared to previously published data from grid-generated turbulence experiments.

Varying ℓ_o produces similar effects to previous results in grid-generated turbulence. It was shown that there exists a region in the downstream decay of scalar variance in a cylinder wake that is well fitted by a power-law. The decay rate of the scalar variance, m , increases as the mandoline is positioned further downstream of the cylinder. The integral length scale of the scalar field decreases as x_θ increases. Therefore, the decay rate can be related to the injection ratio, ℓ_o/L_θ in the same way as it was in grid-generated turbulence. The ratio of the mechanical to thermal time scales, r , is found to slowly decrease downstream of the cylinder. The decay rate of $\langle \theta^2 \rangle$ is found to be proportional to an average r . The peaks of $k_1 \times E_\theta$ do not collapse when the x-axis is normalized by r_{avg} , but do when normalized by m .

Varying the scalar injection scale produces interesting new results. L_θ was varied by varying the width, w , of the mandoline. Varying the spacing of the mandoline's wires did not produce any significant changes in the structure of the scalar field because the variations in the wire spacings were in all cases smaller than ℓ . The decay rate decreases as w is increased, which is similar to increasing the wire spacing (for separations larger than ℓ) in homogeneous isotropic turbulence. In contrast, neither the longitudinal nor the transverse integral length scale of the scalar field were affected by the width of the mandoline. $\ell_{\theta,x}$ and $\ell_{\theta,y}$ were found to be similar.

Moreover, r_{avg} is constant like ℓ_θ . Thus, m and r are independent, which is possible since the budget of $\langle \theta^2 \rangle$ contains two more terms than the budget in homogeneous, isotropic turbulence. The results suggest that ℓ_θ and τ_θ (the thermal time scale) may be fixed by the thermal plume of only one source and that the superposition of other sources does not affect the structure of the scalar field. The most logical reason for this behavior is that the domain of the turbulence cannot be greater than ℓ in this flow.

This result is of interest because it seems to be a property of flows where the integral length scale of the flow is of the same order of magnitude as the domain of the turbulence. In homogeneous and isotropic turbulence, it is possible to create a scalar field that has a larger integral length scale than the velocity field since the domain of the turbulence is several integral length scales wide. This was the case in Warhaft and Lumley[24] when they varied the spacing of their mandoline wires.

In the present case, it is not possible to create a scalar field that has an integral length scale that is larger than the one of the velocity field since it would require the largest scalar eddies to be greater than the domain of the turbulence. In contrast, for a flow with its integral length scale equal to the domain of the turbulence, it is possible to affect the downstream evolution of the scalar field (its decay rate, for example) by changing the scalar injection scale, L_θ . However, this will not change the structure of its field. This result was obtained for only one flow (the wake of a circular cylinder), but should be applicable to many industrial flows, where ℓ is approximately equal to the domain of the turbulence. These flows include jets, mixing layers, boundary layers, wall-bounded shear flows such as channel flow and pipe flow.

Lastly, in contrast with the results obtained in grid-generated turbulence, the anti-correlation between u and θ does not vanish when the mandoline heats the wake. This persisting anti-correlation is because of the structure of the wake. As the mandoline downstream position increases, the magnitude of $\rho_{u\theta}$ decreases because more engulfed, “fast” fluid is heated.

6.1 Future Work

The effect of the scalar injection scale, L_θ , on the decay rate of the scalar variance, m , still requires further investigation. The information is expected to reside in the profile of the wake. The reason for the decoupling of m from the structure of the flow probably lies with the two extra terms of the budget of the scalar variance, which are responsible for removing the constraint $r = m/n$. To study the effects of these two

terms on m and the structure of the scalar field, a detailed analysis of all terms in the budget and their relation to the scalar dispersion across the entire wake is needed.

Another source of information for the decoupling of m from the structure of the scalar field may reside in the structure itself. One of the interesting results is that ℓ_θ is independent of the width of the mandoline, which suggests that it may be fixed by only one heat source. A subsequent experiment of interest would be to measure the dispersion from a single source in the wake and independently vary its transverse location.

Finally, it is the author's conjecture that the independence of m from ℓ/ℓ_θ is a property of flows with ℓ approximately equal to the domain of the turbulence. This hypothesis should be confirmed by performing similar experiments in other flows that corresponds to this description, namely jets, mixing layers, and wall-bounded shear flows such as channel flows or boundary layers.

Appendix A

Accuracy of the IFA300 Constant Temperature Anemometer

The purpose of this appendix is to increase the accuracy of the IFA300 Constant Temperature Anemometer unit by accounting for changes in the environment following calibration. These changes include ambient temperature changes and changes in wire resistance caused by factors other than its temperature.

A.1 Effect of the Operating Resistance

In order to operate the CTA, the experimenter has to properly set 5 parameters. The gain and offset were verified to be accurate and may be changed for convenience. The other three parameters are the cable resistance (R_c), the resistance of the hot-wire at ambient temperature (R_p) and the operating resistance of the hot-wire (R_{op}). The first two parameters are read in by the anemometer. Extra care should be taken to always use the same BNC cable with same hot-wire so that R_c does not change by more than $\pm 0.01\Omega$ from calibration to experiment. R_p is allowed to vary: it is the independent parameter considered here. Usually, the operating temperature of the hot-wire is set using the overheat ratio (α , to be defined later) and R_{op} is obtained by: $R_{op} = \alpha R_p$.

The relative importance of correctly setting R_{op} is shown in Figure A.1. For a $\Delta R_{op} = \pm 0.01\Omega$ (0.1%), which is equal to the precision of the CTA, the corresponding change in velocity output is 1 % while a $\Delta R_{op} = \pm 0.05\Omega$ (0.6%) gives a change in velocity output of about 6 %. This indicates that a given change in R_{op} will produce approximately a corresponding change in velocity which is ten times bigger. Thus, some general guidelines will be developed to ensure the reproducibility from calibration to experiment.

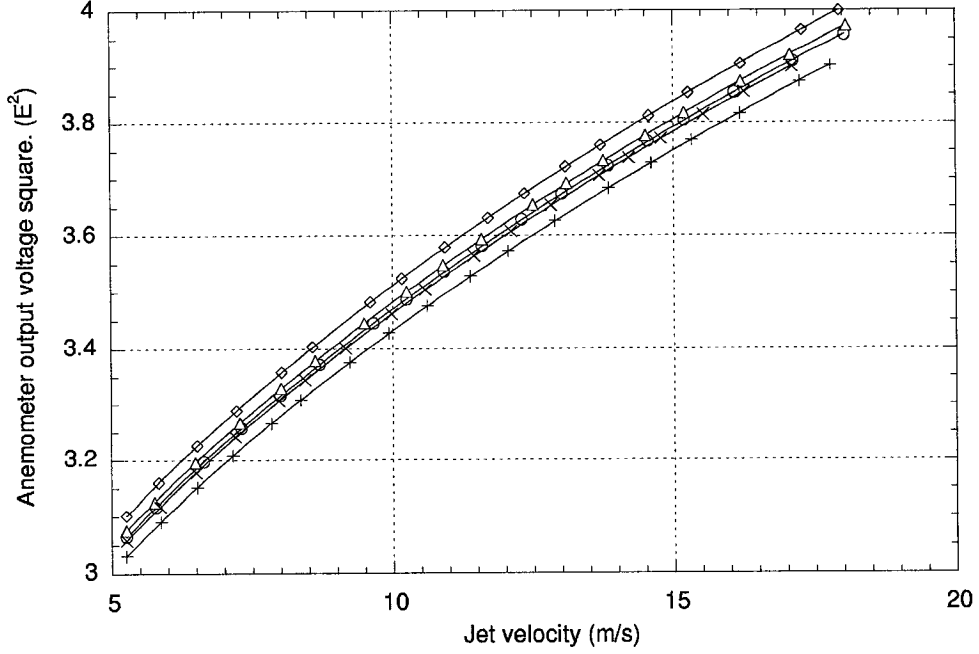


Figure A.1: Effect of R_{op} on velocity output. The jet temperature is constant. \diamond : $R_{op} = 8.89$, \triangle : $R_{op} = 8.85$, \circ : $R_{op} = 8.84$, \times : $R_{op} = 8.83$, $+$: $R_{op} = 8.79$.

A.2 Variations in R_p

While using the same wire for several days, small changes can be observed in the value of R_p as measured by the CTA. At the same time, the ambient temperature in the laboratory can also change (changes are larger in fall and spring when the outside temperature changes most rapidly). At this point, it is important to determine the contributions of ΔR_p from temperature and other factors. In order to do so, a linear relation between wire resistance and its temperature is assumed:

$$R_p = R_o [1 + \beta(T_{flow} - T_o)] \quad (\text{A.1})$$

and

$$\beta = \frac{1}{R_o} \left(\frac{\partial R}{\partial T} \right) \simeq \frac{1}{R_o} \left(\frac{\Delta R}{\Delta T} \right) \quad (\text{A.2})$$

where R_o and T_o are a reference resistance and temperature, respectively, which can be conveniently chosen by the experimenter. β is the thermal resistivity coefficient and is a material property. It can be easily measured using Eq. (A.2) by varying the temperature and measuring the corresponding resistance change. For the material of the hot-wire and for small temperature differences, equation (A.1) holds quite

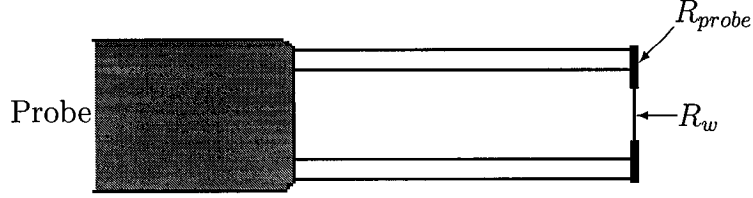


Figure A.2: Schematic of a hot-wire velocity probe.

well. Thus, using (A.1), the change in R_p related to the ambient temperature can be isolated.

Most often, the change in R_p does not correspond to the change indicated by temperature. In addition, some changes in R_p were measured for constant temperatures. Consequently, there must be some other factor in ΔR_p . Before developing any correction factor for α , some assumptions need to be made on the source of ΔR_p .

The extra change in R_p can either come from the wire resistance itself (R_w) or the rest of the probe assembly (R_{probe}). The distinction between the two is important because it makes a difference when computing R_{op} . It is assumed here that all the extra change in R_p comes from R_w only, as it will be shown later that this produces the best accuracy.

A.3 Selecting the Proper Operating Resistance.

A question now arises. What is the proper R_{op} ? In order to answer the question, a series of tests were made. First, the flow temperature was held constant. In Figure A.3, the calibration curves of the same wire are shown for different R_p (different days) keeping R_{op} the same as the starting value (this implies different values for α).

It is clear from Figure A.3 that keeping R_{op} constant is not the best choice because errors as large as 12 % occurs. From the heat transfer point of view, it can be shown that the square of the voltage difference across the wire is related to the velocity of the flow by[51]:

$$E^2 = R_w A_w \left(\frac{T_{w,a} + T_{flow}}{2} \right)^{0.84} (T_{w,a} - T_{flow}) + R_w B_w (T_{w,b} - T_{flow}) U^n \quad (\text{A.3})$$

where A_w and B_w are calibration constants that are specific for a wire. If the temperature of the flow T_{flow} is allowed to vary, the experimenter can get A_w and B_w by varying U and T_{flow} independently. The constants $T_{w,a}$ and $T_{w,b}$ are also obtained from calibration and they represent the operating temperature of the wire.

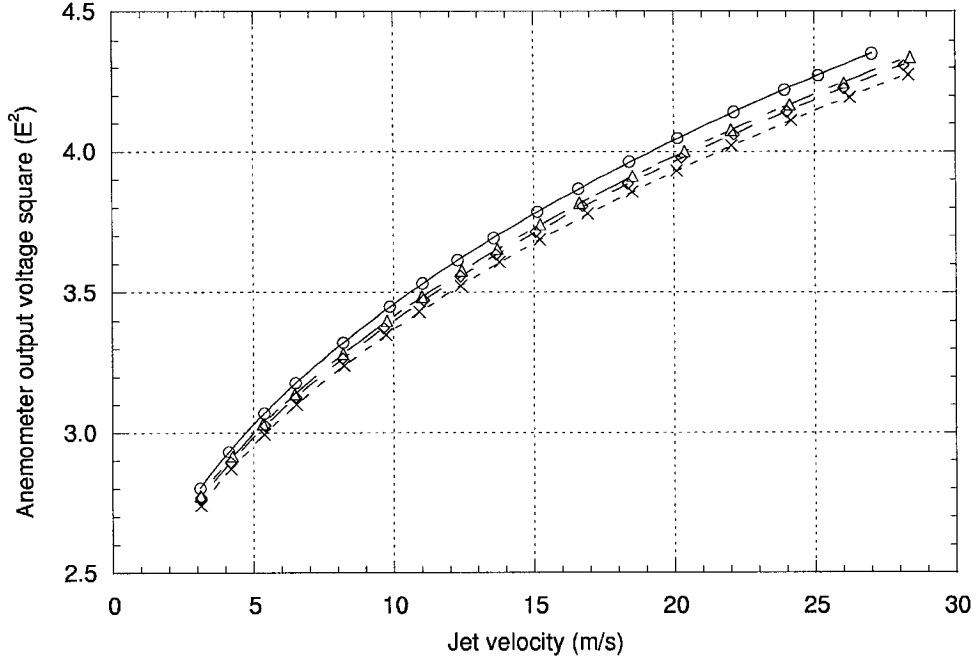


Figure A.3: Calibration curves for a hot-wire keeping its operating resistance constant. \circ : Day 1 ($R_p = 4.83 \Omega$), \triangle : Day 2 ($R_p = 4.84 \Omega$), \diamond : Day 3 ($R_p = 4.84 \Omega$), \times : Day 5 ($R_p = 4.85 \Omega$).

This calibration is cumbersome because the experimenter needs to keep T_{flow} constant for different flow velocities which is not an easy task. In contrast, if the flow is isothermal, the experimenter needs only to calibrate for one T_{flow} and make sure that the temperature difference $\Delta T = T_w - T_{flow}$ is constant from the calibration to the experiment.

A.3.1 Isothermal Flows.

Assuming a linear relation between resistance and temperature, one obtains:

$$R_{op} = \alpha R_p = R_p(1 + \beta \Delta T). \quad (\text{A.4})$$

Clearly, if the thermal resistivity coefficient is constant, then α needs to be constant in order to get the same ΔT . Thus, R_{op} is simply obtained from the measured R_p , keeping α constant.

A.3.2 Non-Isothermal Flows.

In this case, because the calibration accounts for different T_{flow} , it is T_w that needs to be fixed. If the ambient temperature is constant, the same relation as the case

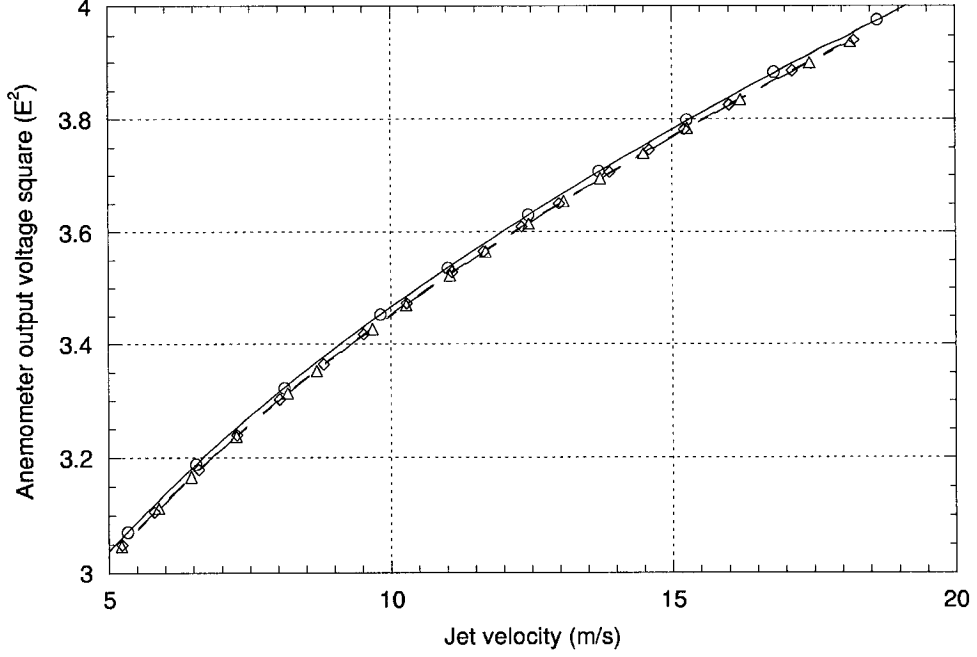


Figure A.4: Calibration curves for a hot-wire keeping its overheat ratio and the flow temperature constant.

of isothermal flow is obtained. A series of calibrations keeping α constant for T_{flow} constant is shown in Figure A.4.

In this case, R_p was changing because the wire was used extensively. An accuracy of 2 % is achieved. This accuracy can be cut by half if R_p is appropriately changed in (A.3). For example:

$$A_{new} = \frac{R_{p,old}}{R_{p,new}} A_{old}. \quad (\text{A.5})$$

For the case where the temperature at which R_p is measured is different from the calibration to the experiment, α needs to be changed in order to keep T_w constant (see equation (A.3). The overheat at experimental conditions can be obtained using (A.1)):

$$R_{op} = \alpha_{T_{calib}} R_{p,T_{calib}} = \alpha_{T_{exp}} R_{p,T_{exp}}. \quad (\text{A.6})$$

In (A.6), $\alpha_{T_{calib}}$ is the overheat ratio at the calibration temperature and is by definition the same as α_{calib} . $\alpha_{T_{exp}}$ is the overheat at the experimental temperature and it is assumed that:

$$R_{p,T_{exp}} = R_{p,T_{calib}} (1 + \beta \Delta T_{Rp}). \quad (\text{A.7})$$

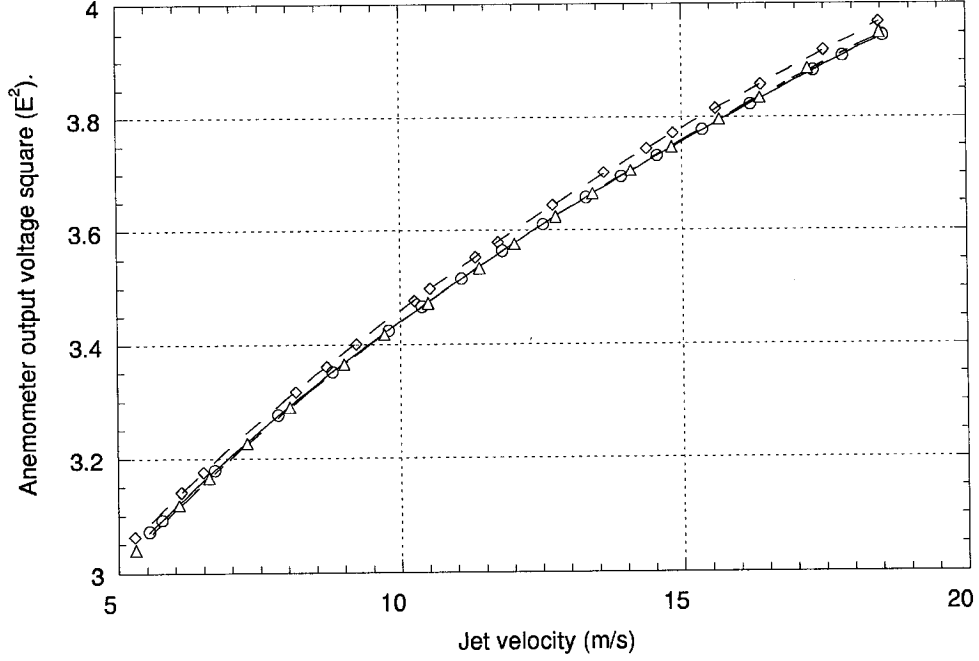


Figure A.5: Calibration curves for a hot-wire at constant flow temperature and adjusting the overheat for changes in ambient temperature.

Consequently, $R_{p,T_{calib}}$ may not be equal to R_p at the calibration day since it can change due to factor other than temperature as previously seen. Using (A.6) and (A.7), $\alpha_{T_{exp}}$ can be obtained:

$$\alpha_{T_{exp}} = \frac{\alpha_{T_{calib}}}{1 + \beta \Delta T_{R_p}} \quad (\text{A.8})$$

where the subscripts “calib” and “exp” denote values measured at calibration and experiment, respectively, and ΔT_{R_p} is the ambient temperature difference from experiment to calibration. Equation (A.8) was tested for a constant flow temperature but with R_p measured at different temperatures. The results are shown in Figure A.5.

For this case, the accuracy is 3 % which is a little bit worse than when R_p was measured at constant ambient temperature but is better than if no correction to α_{exp} was made (which would have produced an error of more than 10 %).

A.4 Rounding Errors

Generally, the accuracy can be increased if the experimenter is careful enough with rounding errors. As it is shown in Figure 1, a variation in R_{op} of $\pm 0.01 \Omega$ creates

an error of 1 %, so if R_{op} is rounded up instead of down, it leads to a small error. Because the settings on the IFA have a precision of 0.01 Ω , the desired α_{calib} may not be achieved exactly. For example, if $R_p = 4.88 \Omega$, setting α to 1.8 gives $R_{op} = 8.784 \Omega$. The value entered on the IFA is thus, 4.78. For experiments, the value of α_{calib} that should be used is $8.78/4.88 = 1.7992$ and not 1.8.

Bibliography

- [1] F. M. White, *Fluid Mechanics*, McGraw-Hill, 4th Ed., McGraw-Hill, Boston, 1999.
- [2] G.K. Batchelor, *An Introduction to Fluid Dynamics*, Cambridge University Press, 1967.
- [3] N.P. Cheremisinoff, *Encyclopedia of Fluid Mechanics*, Gulf Publ. Co, Houston, 1990.
- [4] F.M. White, *Viscous Fluid Flow*, McGraw-Hill, 4th Ed., McGraw-Hill, New York, 1999.
- [5] A. Bejan, *Convection Heat Transfer*, 2nd Ed., Wiley-Interscience, New York, 1995.
- [6] W.M. Kays and M.E. Crawford, *Convective Heat and Mass Transfer*, 3rd Ed., McGraw-Hill, New York, 1993.
- [7] H.L. Swinney, J.P. Gollub, *Hydrodynamic Instabilities and the Transition to Turbulence*, Applied Physics 2nd Ed., Vol. 45, Springer-Verlag, New York, 1985.
- [8] P. Huerre and P.A. Monkewitz, *Local and Global Instabilities in Spatially Developing Flows*, Ann. Rev. of Fluid Mech., Vol. 22, pp. 473, 1990.
- [9] H. Tennekes and J.L. Lumley, *A First Course in Turbulence*, MIT Press, 1972.
- [10] S.B. Pope, *Turbulent Flows*, Cambridge, New York, Cambridge University Press, 2000.
- [11] B.E. Launder and D.B. Spalding, *Mathematical Models of Turbulence*, Academic Press, New York, 1972.
- [12] Z. Warhaft, *Passive Scalars in Turbulent Flows*, Ann. Rev. of Fluid Mech., Vol. 32, pp. 203-240, 2000.

- [13] S. Komori, K. Nagata, Y. Murakami, *Heat and Mass Transfer in a Stable Thermally Stratified Flow*, Dynamics of Atmospheres and Oceans, Vol. 23(1-4), pp. 235-245, 1996.
- [14] P. Moin, K. Mahesh, *Direct Numerical Simulation: A tool in Turbulence Research*, Ann. Rev. of Fluid Mech., Vol. 30, pp. 539-578, 1998.
- [15] M. Lesieur, O. Metais, *New Trends in Large-Eddy Simulations of Turbulence*, Ann. Rev. of Fluid Mech., Vol. 28, pp. 45-82, 1996.
- [16] B.I. Shraiman, E.D. Siggia, *Scalar Turbulence*, Nature, Vol. 405 (6787), pp. 639-646, 2000.
- [17] S. Vaianti, M. Ouldrouis, F. Anselmet, P. Legal, *Statistics of Temperature Increments in Fully-Developed Turbulence.1. Theory*, PHYSICA D, Vol. 73 (1-2), pp. 99-112, 1994.
- [18] H.H. Bruun, *Hot-wire Anemometry: Principles and Signal Analysis*, Oxford University Press, Oxford; New York, 1995.
- [19] F. Moisy, H. Willaime, J.S. Andersen, P. Tabeling, *Passive Scalar Intermittency in Low Temperature Helium Flows*, Phys. Rev. Lett., Vol. 86, no. 21, pp. 4827-4830, 2001.
- [20] S. Deusch and T. Dracos, *Time Resolved 3D Passive Scalar Concentration-Field Imaging by Laser Induced Fluorescence (LIF) in Moving Liquids*, Measurement Science and Technology, Vol. 12, no. 2, pp. 188-200, 2001.
- [21] T. Zhou, R.A. Antonia, L. Danaila, F. Anselmet, *Transport Equations for the Mean Energy and Temperature Dissipation Rates in Grid Turbulence*, Exp. Fluids, Vol. 28 (2), pp. 143-151, 2000.
- [22] T.T. Yeh and C.W. Van Atta, *Spectral Transfer of Scalar and Velocity Fields in Heated-Grid Turbulence*, J. Fluid Mech. Vol. 58, pp. 233-261, 1973.
- [23] R.R. Mills, A.L. Kistler, V. O'Brien, S. Corrsin, *Turbulence and Temperature Fluctuations Behind a Heated Grid*, N.A.C.A. Tech. Note no. 4288, 1958.
- [24] Z. Warhaft and J.L. Lumley, *An Experimental Study of the Decay of Temperature Fluctuations in Grid-Generated Turbulence*, J. Fluid Mech., Vol. 88 (4), pp. 659-684, 1978.

- [25] L.B. Mydlarski and Z. Warhaft, *Passive Scalar Mixing in High Peclet Number in Grid Turbulence in the Presence of a Mean Temperature Gradient*, J. Fluid Mech., Vol. 358, pp. 135, 1998.
- [26] E. M. Kabiri, P. Paranthoen, L. Rosset, J.C. Lecordier, *Temperature Fluctuations and Fluxes Downstream of a Heated Line Source Located in a Turbulent Boundary Layer*, Rev. Gén. Therm., Vol. 37 (3), pp. 181-194, 1998.
- [27] Shen X, Warhaft Z, *The Anisotropy of the Small Scale Structure in High Reynolds Number ($R_\lambda \sim 1000$) Turbulent Shear Flow*, Phys. Fluids, Vol. 12(11), pp. 2976-2989, 2000.
- [28] A. Benaïssa, J. Lemay, F. Anselmet, *Conditional Correlation Between a Passive Scalar and its Dissipation in a Turbulent Boundary Layer*, Exp. Fluids, Vol. 26(6), pp. 488-496, 1999.
- [29] J.Y. Vincont, S. Simoens, M. Ayrault, J.M. Wallace, *Passive Scalar Dispersion in a Turbulent Boundary Layer from a Line Source at the Wall and Downstream of an Obstacle*, J. Fluid Mech., Vol. 424, pp. 127-167, 2000.
- [30] D.V. Papavassiliou and T.J. Hanratty, *Transport of a Passive Scalar in a Turbulent Channel Flow*, Int. J. Heat and Mass Trans., Vol. 40(6), pp. 1303-1311, 1997.
- [31] A.V. Johansson and P.M. Wikstrom, *DNS and Modelling of Passive Scalar Transport in Turbulent Channel Flow with a Focus on Scalar Dissipation Rate Modelling*, Flow Turbulence and Combustion, Vol. 63(1-4), pp. 223-245, 2000.
- [32] J. Mi, R.A. Antonia, *Effect of Large-Scale Intermittency and Mean Shear on Scaling-Range Exponents in a Turbulent Jet - art. no. 026302*, Phys. Rev. E, Vol. 6402 (2), pp. 6302, Part 2, 2001.
- [33] J. Mi, D.S. Nobes, G.J. Nathan, *Influence of Jet Exit Conditions on the Passive Scaler Field of an Axisymmetric Free Jet*, J. Fluid Mech., Vol. 432, pp. 91-125, 2001.
- [34] C.N. Tong, Z. Warhaft, *Passive Scalar Dispersion and Mixing in a Turbulent Jet*, J. Fluid Mech., Vol. 292, pp. 1-38, 1995.
- [35] L.M. Pickett, J.B. Ghandhi, *Passive Scalar Measurements in a Planar Mixing Layer by PLIF of Acetone*, Exp. Fluids, Vol. 31 (3), pp. 309-318, 2001.

- [36] M. Matsumura and R.A. Antonia, *Momentum and Heat Transport in the Turbulent Intermediate Wake of a Circular Cylinder*, J. Fluid Mech., Vol. 250, pp. 651-668, 1993.
- [37] S.H. Kang and C. Meneveau, *Passive Scalar Anisotropy in a Heated Turbulent Wake: New Observations and Implications for Large-Eddy Simulations*, J. Fluid Mech., Vol. 442, pp. 161-170, 2001.
- [38] K. R. Sreenivasan, *Evolution of the Centerline Probability Density Function of Temperature in a Plane Turbulent Wake*, Phys. Fluids, Vol. 24(7), pp. 1232-1234, 1981.
- [39] J. Mi, R.A. Antonia, *Evolution of Centerline Temperature Skewness in a Circular Cylinder Wake*, Int. Commun. Heat Mass Trans., Vol. 26, pp. 45-53, 1999.
- [40] P. Freymuth and M.S. Uberoi, *Structure of Temperature Fluctuations in the Turbulent Wake behind a Heated Cylinder*, Phys. Fluids, Vol. 14, no. 12, pp. 2574-2580, 1971.
- [41] J.C. Larue and P.A. Libby, *Temperature and Intermittency in the Turbulent Wake of a Heated Cylinder*, Phys. Fluids, Vol. 17, No. 5, pp. 873-878, 1974.
- [42] P.M. Wikström, M. Hallböck, A.V. Johansson, *Measurements and Heat-Flux Transport Modelling in a Heated Cylinder Wake*, Int. J. Heat and Fluid Flow, Vol 19, pp. 556-562, 1998.
- [43] L.S.G. Kovasznay, *Hot-Wire Investigation of the Wake Behind Cylinders at Low Reynolds Numbers*, Proc. Roy. Soc. A, Vol. 198, pp. 174, 1949.
- [44] J.A. Ferré and F. Giralt, *Some Topological Features of the Entrainment Process in a Heated Turbulent Wake.*, J. Fluid Mech., Vol. 198, pp. 65-78, 1989.
- [45] R.A. Antonia and L.W.B. Browne, *Anisotropy of the Temperature Dissipation in a Turbulent Wake*, J. Fluid Mech., Vol. 163, pp. 393-403, 1986.
- [46] K.R. Sreenivasan, S. Tavoularis, R. Henry, S. Corrsin, *Temperature Fluctuations and Scales in Grid-Generated Turbulence*, J. Fluid Mech., Vol. 100, part 3, pp. 597-621, 1980.
- [47] P.A. Durbin, *Analysis of the Decay of Temperature Fluctuations in Isotropic Turbulence*, Phys. Fluids, Vol. 25, no 8, pp. 1328-1332, 1982.

- [48] J. Lemay, *Notice d'Utilisation des Anémomètres à Courant Constant (CCA)*., private communication, 2000.
- [49] L.W.B. Browne and R.A. Antonia, *The Effect of Wire Length on Temperature Statistics in a Turbulent Wake*, *Expt. Fluids*, Vol. 5, pp. 426-428, 1987.
- [50] J. Lemay and A. Benaïssa, *Improvement of Cold-Wire Response for Measurement of Temperature Dissipation*, *Exp. Fluids*, Vol. 31, pp. 347-356, 2001.
- [51] J.H. Lienhard V, *The Decay of Turbulence in Thermally Stratified Flow.*, Ph.D. Thesis, Ch. 3.3, University of California, San Diego, 1988.
- [52] L.W.B. Browne, R.A. Antonia, and L.P. Chua, *Calibration of X-Probes for Turbulent-Flow Measurements*, *Exp. Fluids*, Vol. 7, pp. 201-208, 1989.
- [53] H. Rehab, R.A. Antonia, and L. Djenidi, *Streamwise Evolution of a High-Schmidt Number Passive Scalar in a Turbulent Plane Wake.*, *Exp. Fluids*, Vol. 31, pp. 186-192, 2001.
- [54] G. Comte-Bellot and S. Corrsin, *Simple Eulerian Time Correlation of Full- and Narrow-Band Velocity Signals in Grid-Generated 'Isotropic' Turbulence.*, *J. Fluid Mech.*, Vol. 48, pp. 273, 1971.
- [55] A.A. Townsend, *The Passage of Turbulence Through Wire Gauzes.*, *Quart. J. Mech. Appl. Math.*, Vol. 4, pp. 308, 1951.
- [56] E. Lévêque, G. Ruiz-Chavarria, C. Beaudet, S. Ciliberto, *Scaling Laws for the Turbulent Mixing of a Passive Scalar in the Wake of a Cylinder*, *Phys. Fluids*, Vol. 11, No. 7, pp. 1869-1879, 1999.
- [57] J.L. Lumley and H.A. Panofsky, *The Structure of Atmospheric Turbulence*, *Monographs and texts in physics and astronomy*, Vol. 12, 1964.
- [58] A. Sirivat and Z. Warhaft, *The Effect of a Passive Cross-Stream Temperature Gradient on the Evolution of Temperature Variance and Heat Flux in Grid Turbulence.* *J. Fluid Mech.*, Vol. 128, pp. 323-346, 1983.